# Tailoring precipitation/properties and related mechanisms for a high-strength aluminum alloy plate via low-temperature retrogression and re-aging processes

Hou, L. G.; Yu, H.; Wang, Y. W.; You, L.; He, Z. B.; Wu, C. M.; Eskin, D. G.; Katgerman, L.; Zhuang, L. Z.; Zhang, J. S.

**DOI**
10.1016/j.jmst.2021.10.057

**Publication date**
2022

**Document Version**
Final published version

**Published in**
Journal of Materials Science and Technology

Journal of Materials Science & Technology 120 (2022) 15–35

Contents lists available at ScienceDirect

Journal of Materials Science & Technology

journal homepage: www.elsevier.com/locate/jmst

# Tailoring precipitation/properties and related mechanisms for a high-strength aluminum alloy plate via low-temperature retrogression and re-aging processes

L.G. Hou[a,b,d,*], H. Yu[c], Y.W. Wang[a], L. You[a], Z.B. He[a], C.M. Wu[d], D.G. Eskin[b,e,*], L. Katgerman[f,g], L.Z. Zhuang[a,*], J.S. Zhang[a]

[a] State Key Laboratory for Advanced Metals & Materials, University of Science & Technology Beijing, Beijing 100083, China
[b] BCAST, Brunel University London, Kingston Lane, Uxbridge Middlesex UB8 3PH, United Kingdom
[c] Institute of mineral resources, Chinese Academy of Geological Sciences, Beijing 100037, China
[d] Nanjing Advanced Transportation Equipment New Technology Research Institute, Nanjing 211800, China
[e] Tomsk State University, Tomsk, 634050, Russian Federation
[f] Katgerman Aluminium Technology, van Beuningenlaan 10, 2334CC Leiden, Netherlands
[g] Department of Materials Science and Engineering, Delft University of Technology, Mekelweg 2, 2628CD Delft, the Netherlands

ARTICLE INFO

*Article history:*
Received 25 August 2021
Revised 21 October 2021
Accepted 21 October 2021
Available online 9 March 2022

*Keywords:*
Aluminum alloy
Heat treatment
Precipitation
Strength
Grain boundary

ABSTRACT

The retrogression and re-aging (RRA) processes, aimed mainly at tailoring intergranular precipitates, could significantly improve the corrosion resistance (i.e., stress corrosion cracking resistance) without considerably decreasing the strength, which signifies that an efficient control of the size, distribution and evolution of intergranular and intragranular precipitates becomes critical for the integrated properties of the (mid-)thick high-strength Al alloy plates. Compared to RRA process with retrogression at 200 °C (T77), this study investigated the impact of a modified RRA process (MT77) with lower retrogression temperatures (155-175 °C) and first-stage under-aging on the properties of a high-strength AA7050 Al alloy, in combination with detailed precipitate characterization. The study showed that the strength/microhardness of the RRA-treated alloys decreased with raising retrogression temperature and/or prolonging retrogression time, along with the increased electrical conductivity. The rapid responsiveness of microstructure/property typical of retrogression at 200 °C was obviously postponed or decreased by using MT77 process with longer retrogression time that was more suitable for treating the (mid-)thick plates. On the other hand, higher retrogression temperature facilitated more intragranular $\eta$ precipitates, coarse intergranular precipitates and wide precipitate free zones, which prominently increased the electrical conductivity alongside a considerable strength loss as compared to the MT77-treated alloys. With the preferred MT77 process, the high strength approaching T6 level as well as good corrosion resistance was achieved. However, though a relatively homogeneous through-thickness strength was obtained, some small discrepancies of properties between the central and surface areas of an 86-mm thick 7050 Al alloy plate were observed, possibly related to the quenching sensitivity. The precipitate evolution and mechanistic connection to the properties were discussed and reviewed for high-strength Al alloys along with suggestions for further RRA optimization.



## 1. Introduction

Integrated properties including strength, fatigue/toughness and corrosion resistance of Al-Zn-Mg-Cu (AA7XXX-series) alloys and other precipitation strengthened alloys can be highly improved by precipitate control (i.e., type, size, shape, distribution, etc.)[1–6]. The precipitation sequence of Al-Zn-Mg-Cu series alloys is generally recognized as follows[1·3·4·6]: supersaturated solid solution (SSS) → atomic clusters or GP I/II zones → $\eta'$ → $\eta$, where both GP I/II zones and $\eta'$ phase are metastable precursors of the equilibrium incoherent $\eta$-$MgZn_2$ phase with a hexagonal structure. Generally, the peak aging of AA7XXX series Al alloys (normally T6 temper) results in the precipitation of coherent

* Corresponding authors:
*E-mail addresses:* lghou@skl.ustb.edu.cn (L.G. Hou), Dmitry.Eskin@brunel.ac.uk (D.G. Eskin), lingzhongzhuang@yahoo.com (L.Z. Zhuang).

https://doi.org/10.1016/j.jmst.2021.10.057
1005-0302/

GP zones and the coherent/semi-coherent $\eta'$ phase for maximizing the strength but with inferior corrosion resistance (i.e., intergranular corrosion (IGC) and stress corrosion cracking (SCC))[7–11], hindering their application in critical structural frames or components in aerospace/aviation and ground transportation. Alternative over-aging processes typical of a two-step T73/T74 temper were intentionally developed to improve the corrosion resistance but unfortunately with a loss of 10%-15% strength relative to T6 state[12–14] because of the growth/coarsening and/or discontinuity of intragranular/intergranular precipitates. However, the advanced retrogression and re-aging (RRA) process developed by Cina could help achieve high strength similar to that of T6 state and concurrently preferable SCC resistance similar to that of T73 state via efficient control of intragranular/intergranular precipitates[15·16]. Already, the RRA processes were proved to effectively balance the strength and corrosion resistance for high-strength Al-Zn-Mg-Cu series alloys[17–22], i.e., the T77 process (three-step aging) developed by Alcoa[23–25]. However, the corrosion resistance being dependent on many factors, such as solute segregation, precipitation free zones (PFZs) near grain boundaries (GBs), grain boundary precipitates (GBPs)[26] and in-service conditions, could be significantly affected by alloy composition and heat treatments.

With intragranular fine GP zones and $\eta'$ precipitates responsible for high strength, the continuous GBPs are rooted as the key reason for high SCC sensitivity of the T6-aged Al-Zn-Mg-Cu series alloys, which could promote continuous corrosion paths along GBs because of their different corrosion potentials compared to the Al matrix (including PFZs)[8·10·11]. On coarsening upon over-aging, these GBPs become discontinuous, along with the growth of intragranular precipitates[2]. By using an RRA process, both discontinuous GBPs and intragranular dispersed GP zones/$\eta'$ precipitates can be simultaneously obtained with good corrosion resistance and high strength[27·28]. The retrogression treatment as a critical RRA step can partially or completely dissolve intragranular GP zones and fine $\eta'$ precipitates caused by normal first-step peak aging (or T6 temper, i.e., 120 °C-24 h), while promoting the transformation of some intragranular $\eta'$ precipitates into stable $\eta$ phase as well as the growth of GBPs[27]. Thus, sufficiently high retrogression temperature[26] may greatly curtail the retrogression time, i.e., a few seconds to minutes at 200 °C or above[29·30]. On the other hand, by using lower retrogression temperature and longer retrogression time (i.e., 180 °C/60 min), higher fracture toughness and similar electrical conductivity to that of the T74 state were obtained for a 7B04 Al alloy plate (thickness: 40 mm) with a strength approaching that of the T6 state[31]. An RRA or a double RRA process (retrogressed at 180 °C) were applied to a 7B50 Al alloy plate (thickness: 20 mm) to achieve similar strength and higher exfoliation corrosion (EXCO) resistance compared to the T76 state[32·33]. An RRA process with 170 °C/60 min retrogression treatment improved the strength and EXCO resistance of an extruded AA7249 Al alloy profile (thickness: ~20 mm) relative to that after T6 treatment[19]. Although an RRA process with retrogression at 200 °C can contribute to a higher strength for an AA7075 Al alloy, much better SCC resistance can be achieved with low-temperature and long-time retrogression treatments (i.e., 160 °C/250 min or 160 °C/660 min)[34·35]. Thus, the RRA process with low retrogression temperatures can improve SCC resistance with strength similar to that of the T6 state and facilitate long-time retrogression treatments (i. e., for some hours). It may be considered that the insufficient dissolution of $\eta'$ precipitates during low-temperature retrogression may impair the final properties[36], but the RRA process with low retrogression temperatures would be applicable to the (mid-)thick plates compared to the T77 process with high retrogression temperature (i.e., above 200 °C). Other factors need to be also taken into account, such as the segregation or alloying levels[37–40], i.e., increasing Cu content benefits corrosion resistance of high-strength Al alloys[41].

It is known that the alloy electrical conductivity can be affected by electron scattering induced by GP zones and/or precipitates[42] and used to evaluate the effects of precipitate variation on SCC resistance of high-strength Al alloys, i.e., the higher the electrical conductivity, the better the SCC resistance[43–46], in comparison with low-strain rate tension and static tensile methods. An effective RRA process and precise composition/processing control are required for achieving better integrated properties and ensuring the consistency of different batches for high-strength Al-Zn-Mg-Cu series alloy plates. For instance, the electrical conductivity of an original AA7050 Al alloy plate used in this study was ~29% IACS (International Annealed Copper Standard), attesting to poor SCC resistance (the electrical conductivity ≥38% IACS corresponds to acceptable EXCO/SCC resistance[46]). This study aims at investigating the effects of an RRA treatment with low retrogression temperature (155-175 °C) on microstructures and properties of an AA7050 Al alloy, namely a modified T77 (MT77) process, in comparison to normal T77 process retrogressed at 200 °C, in a bid to achieve good combination of matrix precipitates, GBPs, PFZs, etc. This process can be used for the treatment of (mid-)thick Al-Zn-Mg-Cu series alloy plates or extruded/forged components that require higher corrosion resistance and strength in different applications such as aerospace/airplane or transportation.

## 2. Experimental

The samples (15 mm × 15 mm × 120 mm) cut at similar positions from a commercial hot-rolled AA7050 Al alloy plate (thickness: 80 mm, composition: Al-5.7Zn-1.9Mg-2.0Cu-0.1Mn-0.04Cr (wt%)) were solution treated at 475°C (± 2°C) for 120 min in an electric furnace and then quenched into water (~25°C) with a quenching transfer time less than 5 s. The as-received AA7050 Al alloy contained many coarse particles such as $Al_7Cu_2Fe$ and $S$-$Al_2CuMg$, as shown by SEM images in Fig. S1. Then these samples were aged with three processes: (1) T6 temper: 120°C/1440 min with air cooling, (2) T77: 120°C/1440 min+200°C/$t$ min + water cooling + 120°C/1440 min, (3) MT77: 120°C/300 min + (155~175°C)/$x$ min + 120°C/1440 min. The second and third processes were marked by T77 (200°C/$t$ min) and MT77 ($T$°C/$x$ min), respectively, with $t$ and $x$ being variables. Then, a three-step solution treatment (475°C/60 min + 480°C/10 min + 485°C/10 min) was performed with subsequent T6 temper (marked as T6*) and MT77 process. After the first-step aging during the T77/MT77 processing, the samples were directly heated to the second-step temperature within ~30 min. After the second-step aging or retrogression treatments, the samples were furnace-cooled to 120°C for the third-step aging during the MT77 processing, while some samples were air-cooled to room temperature with subsequent T6 aging. Based on the higher strength and electrical conductivity approaching or exceeding 38% IACS, the optimal MT77 process was applied to an ~86 mm thick AA7050 Al alloy plate.

Three parallel rod specimens (5 mm dia., 25 mm gauge length, as shown in Fig. S1) cut from similar thickness position were used to measure mechanical properties in an MTS 810 material testing machine (strain rate: 1 mm/min). Microhardness (HV) values were averaged from 7 tests without maximum/minimum values by using an HV-5 Vickers hardness tester with a 2.942 N load and 30s duration. The electrical conductivity was measured by a 7501A eddy current electrical conductivity tester. IACS was used to express electrical conductivity, which meant that the electrical conductivity of annealed unalloyed Cu (resistivity: $1.73 \times 10^{-8}$ Ω m) can be considered as 100 IACS % and the conductivity of other alloys can be expressed as a percentage to it.

The microstructures were observed in a scanning electron microscope (SEM, ZEISS SUPRA 55, voltage: 15 kV, working distance: 18-25 mm). A JEM-2010 high resolution transmission electron microscope (HRTEM, 200 kV) and an FEI Tecnai F20 transmission electron microscope (TEM, 200 kV) were used to characterize the precipitates. The selected area electron diffraction (SAED) patterns along $[001]_{Al}$, $[110]_{Al}$ and $[112]_{Al}$ zone axes were obtained for identifying precipitates (mainly intragranular precipitates) with typical diffraction patterns after different treatments. The DigitalMicrograph software was used to analyze the HRTEM data. SEM samples were ground and polished to mirror surfaces without any etching. Samples with 1 mm thickness cut from the treated alloys were ground to ~80 $\mu$m thickness by using sand papers (800# - 2000#) and then disks with 3 mm diameter were punched for twin-jet electro-polishing by using an electrolyte with $HNO_3$: $CH_3OH$=3: 7 at −20°C – −30°C (voltage: 10–15 V, current: 60–70 mA). The length and width of each precipitate were measured individually from the TEM bright field and HRTEM images by ImageJ software (https://imagej.nih.gov/ij/) and given with a range in Table S1, while the diameters of some precipitates were calculated from an equivalent circle with same area. The statistical precipitate numbers are shown in Fig. S2.

According to the ASTM G110 accelerated immersion test, the L-T plane samples at the 1/4 thickness position were used for IGC tests. Before testing, the sample surfaces were ground to 1200 $\mu$m in ethanol, ultrasonically cleaned and air-dried, and then the samples were immersed in the etching solution (50 mL Nitric Acid (70%) + 5 mL HF (48%) + 945 mL deionized water, 93°C) for 1 min, rinsed with deionized water; subsequently the samples were immersed in concentrated nitric acid (70%) at room temperature for 1 min, rinsed with deionized water and air dry. Later, the samples were immersed in the solution (57 g NaCl + 10 mL $H_2O_2$ (30%) + 990 mL deionized water, 30±3°C) for 6 h, and then cleaned in deionized water with removing loose corrosion products and air dried. The corroded samples were cut and polished along their cross sections, and the corrosion depths were observed and measured by using an Olympus GX51 optical microscope.

## 3. Results and discussion

### 3.1. Mechanical properties

The room-temperature mechanical properties of the T6- and RRA-treated AA7050 Al alloys in Fig. 1(a, b) show that the yield strength (YS) and ultimate tensile strength (UTS) of the T77-treated alloy (retrogression temperature: 200°C) decrease with retrogression time (elongations: 8%-10%) in comparison with those of the T6/T6* state. Compared to the one-step solution treatment, the three-step solution treatment with higher temperature can promote sufficient dissolution of precipitates (i.e., $\eta'$ and $\eta$ phases) as well as some constitutive particles (i.e., S-$Al_2CuMg$) for a higher solute supersaturation[3·6], facilitating an enhanced precipitation hardening ability of T6* state. When retrogressed at 155 °C for 300 min in the MT77 process, the YS and UTS increase slightly relative to that of T6* state. With extending retrogression time to 600 min or 900 min, the strength/HV continuously declines. When retrogressed at 160 °C (MT77), the HV and UTS decrease with retrogression time but YS increases after 300 min retrogression. After retrogression at 165 °C for 300 min (MT77), YS and UTS increase slightly relative to T6* state, but then the strength/HV decreases sharply till 600 min retrogression time (elongation: 7.8%-12%). Although properties of the T77-treated AA7050 Al alloy are below reference values[9] (at the same retrogression temperature but with higher Zn, Mg and Cu concentrations as well as very low Fe and Si amounts, which could cause slightly different mechanical properties), the properties of MT77 (155/160/165 °C-300 min) alloy are close to them. Regardless of the effects of alloy compositions, the MT77 process displays a noticeable potential to improve the mechanical properties.

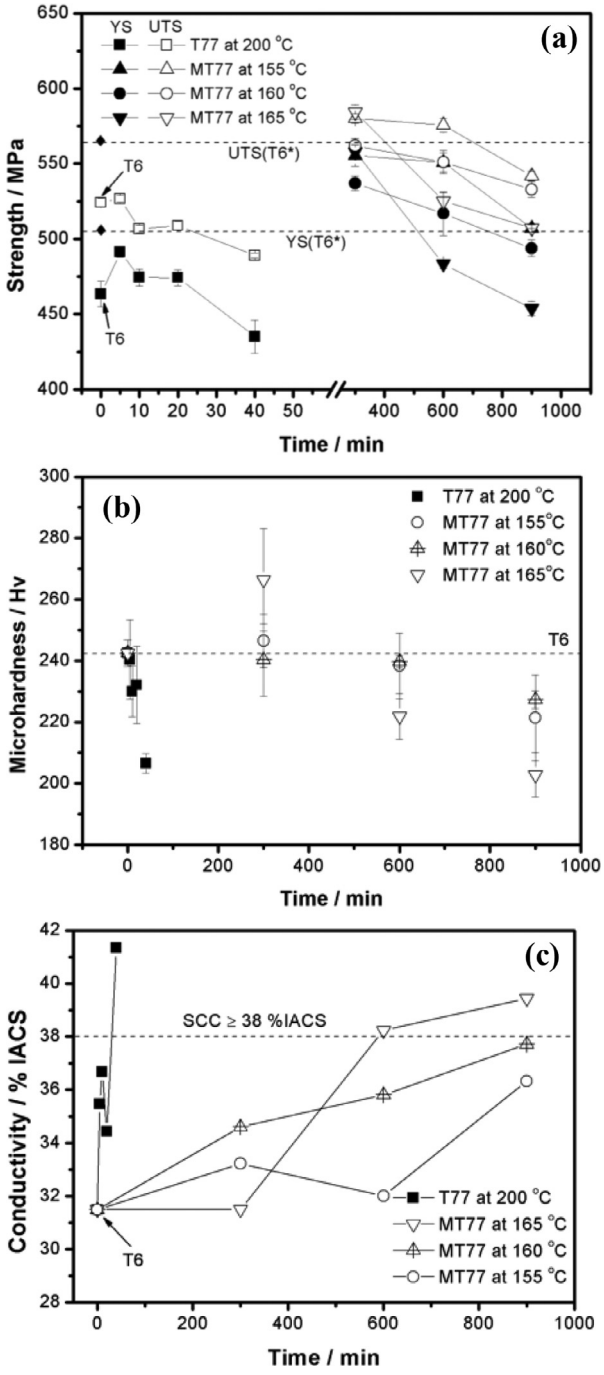


**Fig. 1.** Strength (a), microhardness (b) and electrical conductivity (c) of AA7050 Al alloys after T6 (time=0 min), T77 and MT77 treatments.

Some additional RRA treatments were performed as follows. (1) After 165 °C/300 min (MT77) retrogression treatment, long-time (735 min)/short-time (135 min) air cooling was used to approach room temperature following a third-step aging (at 120 °C). It shows that both YS and UTS with short-time air cooling decrease slightly, in comparison with those of the T6* state, but YS somewhat increases (~ 10 MPa) while UTS decreases (~ 19 MPa) with long-time air cooling. Compared to those of MT77 (165 °C/300 min) process without air cooling, both YS and UTS decrease by using air cooling, but with long-time air cooling the strength was close

to that of the T6* state. (2) With three-step solution treatment, the MT77 (155 °C/300 min) alloy displays slightly increased YS (~ 11 MPa increment) and similar UTS compared with that after using one-step solution treatment. (3) For MT77 (160 °C/300 min) process, prolonging its third-step aging time to 2160 min (at 120 °C) decreases YS and UTS in comparison with those of the T6* state. (4) After one-step solution treatment, four-days natural aging is used before MT77 (160 °C/300 min) process. This decreases the final strength, slightly lower than that of the T6* state, i. e., ~10 MPa YS and ~30 MPa UTS reductions. It is revealed that the application of natural aging after solution treatment, air cooling after retrogression treatment or extending aging time without directly shifting the plates into subsequent furnaces may facilitate practical operation.

### 3.2. Electrical conductivity

The variations of electrical conductivity of high-strength Al alloys during solution and aging treatments can be correlated with the precipitates (i.e., GP-zones, $\eta'$ and $\eta$ phases) and the solute concentration in the matrix[42·43·47]. Specifically, the aging treatments can affect alloy's electrical conductivity in two ways[42]: (1) reducing the supersaturation of the matrix could decrease lattice distortion and weaken scattering to electrons leading to increased electrical conductivity; (2) the precipitation of coherent GP-zones and $\eta'$ phase distorts Al matrix and causes additional scattering to electrons, thus decreasing electrical conductivity. Overall, with higher aging temperature and longer time, sufficient precipitation will deplete solutes in Al matrix and electrical conductivity will increase Fig. 1.(c) shows that the electrical conductivity of the T77-treated alloys increases with retrogression time besides a slight reduction after 20 min retrogression treatment (with a little change of strength). This means that numerous precipitates (see Section 3.3) can lead to a stronger scattering effect to electrons than the impact from the reduction of solute solubility in Al matrix[43–46]. Further increasing retrogression time can additionally promote the precipitation (see Section 3.3) and decrease the supersaturation in Al matrix. As a result, the scattering effect induced by the solute atoms would be greatly reduced, thus raising the electrical conductivity to 41.4% IACS after T77 (200 °C/40 min) treatment, much higher than that of T6 state. But the strength and hardness are lower than those of the T6 state, demonstrating that enhancing the electrical conductivity (corrosion resistance) goes along with the strength loss.

Fig. 1(c) further shows that the electrical conductivity of the MT77 (155 °C/300 min) alloy (33.3% IACS) is higher than that of the T6 state, and can be increased to 36.4% IACS after 900 min retrogression treatment, arising from the precipitation of coherent/incoherent precipitates and the reduction of matrix solubility[42–46]. Moreover, when retrogressed at 160/165 °C, the electrical conductivity increases to 37.8% IACS (MT77 (160 °C/900 min)), 38.3% IACS (MT77 (165 °C/600 min)) and 39.5% IACS (MT77 (165 °C/900 min)) with the strength similar to that of T6 state, leading to better corrosion resistance[46]. Prolonging the third-step aging time or using natural aging before MT77 treatment can also raise electrical conductivity to above 38% IACS. The constituent intermetallics[48·49] (as shown in Fig. S1) have little influence on alloy's electrical conductivity. Factors, such as interfacial electron scattering and the reduction of solute concentration in Al matrix (i. e., Cu and Mg atoms forming S phase), are not usually considered for the assessment of electrical conductivity. The results show that the electrical conductivity of the MT77 (160 °C/900 min) alloy can meet the requirement (≥38% IACS) along with YS being close to that of T6 state, being comparable to those of the MT77 (165 °C/600 min) alloy. The MT77 (165 °C/900 min) process can enhance the electrical conductivity to 39.5% IACS but with a lower YS. Thus, for better corrosion resistance and minimum strength loss, both MT77 (160 °C/900 min) and MT77 (165 °C/600 min) processes look preferred.

### 3.3. Precipitates in the T77- and MT77-treated alloys

#### 3.3.1. Intragranular precipitates

*3.3.1.1. T77 process with retrogression at 200 °C.* Fig. 2(a) shows uniformly distributed precipitates with the size 5-10 nm in the T6 state, which are verified as GPI zones by weak diffraction spots at $\{1,(2n+1)/4,0\}_{Al}$ positions, and as $\eta'$ phase by diffraction spots at $1/3\{220\}_{Al}$ and $2/3\{220\}_{Al}$ positions (Fig. 2(b)). This is in accordance with previous studies that the T6 aged alloys are mainly strengthened by GP zones and $\eta'$ phase[2·50·51]. This not only causes a significant lattice distortion (or strain) to impede dislocation moving leading to a higher strength but also induces strong scattering effects to electrons, leading to a lower electrical conductivity or inferior corrosion resistance[52] Fig. 2.(c) shows that the intragranular precipitates in the T77-treated alloy (retrogressed for 5 min) are similar to those of T6 state (Fig. 2(a)) or with slight coarsening. The diffraction streaks along $1/3\{220\}_{Al}$ and $2/3\{220\}_{Al}$ positions and diffraction spots at $1/2\{311\}_{Al}$ position correspond to $\eta'$ phase and GPII zones (Fig. 2(d). Prolonging the retrogression time to 40 min (at 200 °C) causes coarsening of the precipitates (Fig. 2 (e, g) and Table S1) Fig. 2.(f) indicates that there is no contrast at $\{1,(2n+1)/4,0\}$ position but an obvious contrast at $1/3\{220\}_{Al}$ and $2/3\{220\}_{Al}$ positions corresponding to $\eta'$ phase, as well as the diffraction spots of $\eta$ phase (i.e., different contrast at $2/3\{220\}_{Al}$ position), which means that GP zones disappear in the T77 (200 °C/40 min) alloy. Obviously, the corresponding precipitation occurs as the T77 process retrogressed at 200 °C, i. e., the dot-like GP zones and $\eta'$ phase in the T77 (200 °C/5 min) alloy are replaced by larger $\eta'$ and $\eta$ precipitates in the T77 (200 °C/40 min) alloy. As a consequence, the strength of the T77 (200 °C/5 min) alloy approaching that of the T6 state is greatly reduced after T77 (200 °C/40 min) treatment (Fig. 1(a)), similar to previously reported RRA processing[15·16]. Even though the higher electrical conductivity or corrosion resistance can be gained in the T77-treated alloys (i.e., > 38% IACS), their strength is lower than that of the T6 state. Notwithstanding the alloy strength can be lowered by the T77 process with short-time retrogression, which cannot be applicable to (mid-)thick plates because the short retrogression time cannot ensure sufficient heating in the plate center. Furthermore, the FFT images of regions 1, 2 and 5 (Fig. 2 (h, j)) exhibit similar diffraction features that correspond to GPII zones with almost disc-like morphologies. And the IFFT images of regions 1 and 2 show an obvious contrast but complete coherency with Al matrix. The FFT image of region 4 (Fig. 2(j)) exhibits diffraction features of $\eta'$ phase with obvious structure fluctuation. The FFT image of region 3 in Fig. 2(i) displays similar feature to previously reported result[53], corresponding to $\eta$ phase with an orientation relationship as $(0001)_{\eta}//(1\bar{1}0)_{Al}$, $[10\bar{1}0]_{\eta}//[00\bar{1}]_{Al}$. Its IFFT image shows $d(0001)_{\eta}$=0.838 nm≈$3d(110)_{Al}$ ($d(110)_{Al}$= 0.2804 nm) and Fig. 2 (i1) further indicates that the bright atoms might be multi-layer stacked Zn atoms with larger Z number. Also, the FFT image of region 6 in Fig. 2(j) may represent $\eta$ phase according to ref [54]. Compared to the higher T6 peak strength mainly caused by $\eta'$ precipitates and GP zones, the obvious strength reduction after T77 (200 °C/40 min) treatment could reflect the over-aging state that is intimately connected with the coarsened precipitates, especially the formation of stable $\eta$ phase. Thus, it is considered that $\eta'$ and $\eta$ phases are dominated in the T77 (200 °C/40 min) alloy along with few GPII zones.

*3.3.1.2. MT77 processes with retrogression at 155/165/175 °C for 300 min.* The above data indicate that the T77 process with 200 °C as

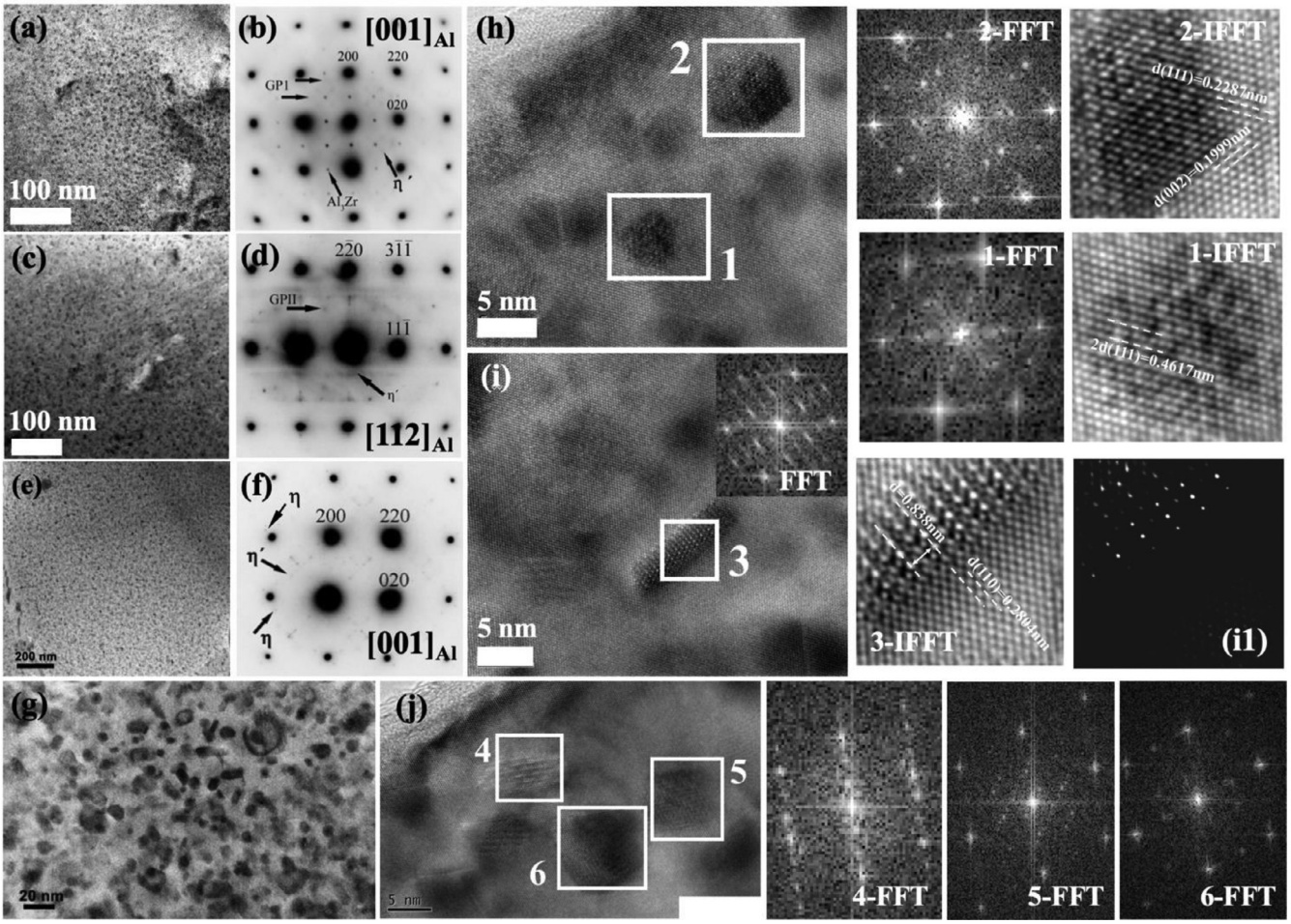


**Fig. 2.** Intragranular precipitates (a, c, e, g), related selected area electron diffraction (SAED) patterns (b, d, f) and HREM images (h-j) of the T6- (a, b) and T77-treated alloys: (c, d) T77 (200 °C/5 min), (e-g, h-j) T77 (200 °C/40 min). Fast Fourier Transform (FFT) images of regions 1-6 in (h-j) correspond to 1-FFT to 6-FFT, respectively. The IFFT images of regions 1, 2 and 3 are also given. (i1) after adjusting brightness and gamma values of IFFT image of region 3 that can display bright contrast. The diffraction spots of $Al_3Zr$ phase with $L1_2$ superlattice structure also appear in (b, d, f).

retrogression temperature cannot guarantee practical controls for (mid-)thick plates because of its rapid precipitation responsiveness that should be retarded/weakened with prolonging operating time, and low-temperature retrogression needs to be explored Fig. 3. (a, b) shows that after retrogression at 155 °C for 300 min (MT77 (155 °C/300 min) process), abundant short-rod and/or granular precipitates are uniformly distributed in the matrix (see statistic sizes in Table S1 and Fig. S2) Fig. 3. (c, d) shows the appearance of typical diffraction spots of $\eta'$ phase ($1/3\{022\}_{Al}$ and $2/3\{022\}_{Al}$) and the superimposed diffraction spots of $\eta$ phase. The diffraction streaks along $\{111\}_{Al}$ correspond to GPII zones. Thus, $\eta'$ phase and GPII zones are formed in the MT77 (155 °C/300 min) alloy, possibly with a few $\eta$ precipitates Fig. 3.(e) shows a disc-like GP zone with dumbbell-like atomic arrangement (Fig. 3(e3)). Compared with the (200) diffraction pattern of the matrix, the (200) diffraction pattern of this GP zone is split (as inserted in Fig. 3(e)). This may be an artifact induced by FFT processing, but it may also point out that the localized lattice strain may be caused by the substitute of Al lattice, demonstrating a coherent GP zone. Furthermore, Fig. 3 (e2) also shows diffraction streaks along $\{111\}_{Al}$, signifying the appearance of atom clusters/aggregates such as GPII zones attached to $(1\bar{1}1)_{Al}$ plane (Fig. 3(e4)), which is stacked with two types of atoms via single and double layers. The bright single atom layer is Zn-rich while the dark double layer is Mg-/Al-rich[55], and this GPII zone would be in its infancy. The adjacent GPII zone attached to $(11\bar{1})_{Al}$ plane exhibits localized strain induced by multi-layer atom stacking, as a result an obvious virtual image appears after IFFT processing, indicating an interim stage of GPII zone. For the superimposition of GPII zones, their inner atoms are rearranged and start to transform into metastable $\eta'$ phase, which is reflected in diffraction streaks in FFT image: gradually transitioning to sharp diffraction spots Fig. 3.(f) and related FFT images also demonstrate the formation of GPII zones and $\eta'$ phase in the MT77 (155 °C/300 min) alloy, with precipitates 1.3-2.5 nm wide belonging to GP zones while the wider ones being regarded as $\eta'$ phase. Furthermore, the FFT image of Fig. 3 (g) exhibits diffraction streaks along $\{111\}_{Al}$ and the white regions 2-4 display coherency with Al matrix as well as yellow-marked precipitates, partially showing lattice unmatching because of dislocation aggregation. Particularly, the aggregation and growth of multiple coherent structures can cause lattice distortion within phases. The FFT image of coherent white region 2 (Fig. 3(g)) displays diffraction streaks along $\{111\}_{Al}$ and linear different features perpendicular to $1/3\{220\}_{Al}$ and $2/3\{220\}_{Al}$ ($[112]_{Al}$ zone axis), but the diffraction pattern of white region 3 does not overlap with that of $\eta'$ phase (Fig. 3(g1)), which can be deduced as a transition stage from a maturing GP zone to $\eta'$ phase, but still identified as GPII zone. And the corresponding IFFT image indicates the appearance of a dislocation in this GPII zone that may move it towards semi-coherent relationship. With the growth of GPII zones, this linear diffraction features become separate diffraction spots and the dense diffraction pattern of $\eta'$ phase (Fig. 3 (g1)) shows multiple linear diffrac-

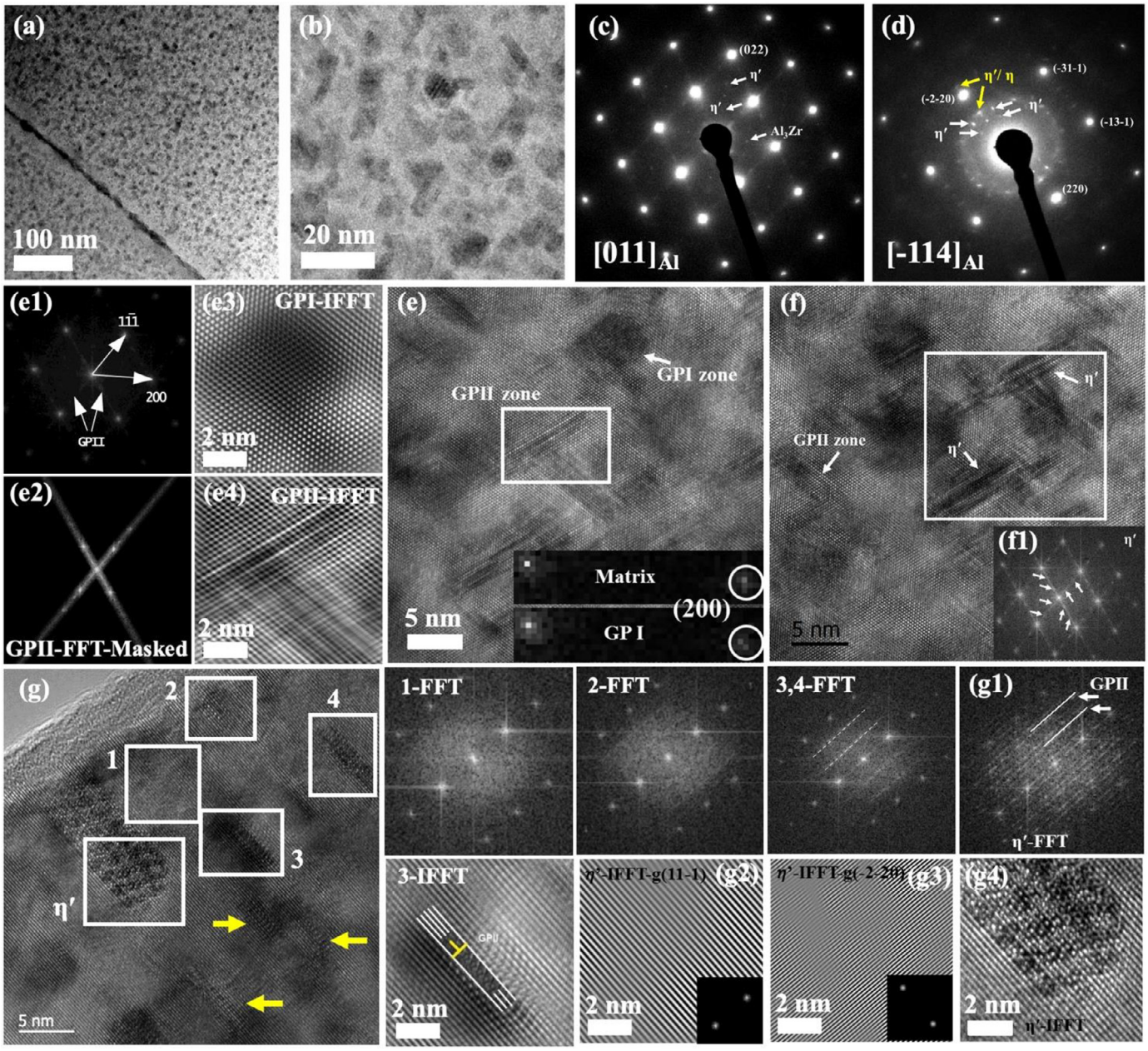


**Fig. 3.** Intragranular precipitates in the MT77 (155 °C/300 min) alloy: (a, b) TEM image, (c, d) SADE pattern, (e-g) HREM images. (e1) FFT images of the white region in (e), (e2) masked FFT image of GP II zone in (e), (e3) IFFT images of GP I zone in (e), (e4) IFFT images of (e3), (f1) FFT images of white region in (f). (g1) FFT image of $\eta$' phase in (g), (g2) and (g3) are IFFT images along $g(11\bar{1})_{Al}$ and $g(\bar{2}\bar{2}0)_{Al}$ of (g1), (g4) IFFT image of (g1). The FFT/IFFT images of white regions 1-4 in (g) are shown with corresponding numbers. The yellow-marked precipitates also display similar morphology with white region 3 in (g).

tion features along $\{111\}_{Al}$, which do not overlap with that of GPII zone and can reflect atom/vacancy rearrangement within $\eta'$ phase, directly proving a transformation from aggregated GPII zones into $\eta'$ phase. However, its structure do not match well previous results[50·53·54·56], possibly being the $Mg_{32}(Al,Zn)_{49}$ phase with a BCC structure [53·57·58] Fig. 3. (g3, g4) indicates that an $\eta'$ precipitate stacked along $\{111\}_{Al}$ is almost coherent along $(111)_{Al}$ plane. Apparently, the diffraction streaks of GPII zones are parallel with those of $\eta'$ phase, revealing GPII zone as a precursor of $\eta'$ phase.

Similarly, Fig. 4 (a, b) shows numerous short-rod and fine spherical precipitates in the MT77 (165 °C/300 min) alloy and the SAED patterns display diffraction spots of $\eta'$ phase (arrow-marked) along with a few overlaid spots of $\eta$ phase (Fig. 4 (c-e)). Weak diffraction spots at $1/2\{311\}_{Al}$ position are in line with GPII zones, as yellow-marked in Fig. 4(e). These data reveal that GPII zones, $\eta'$ and $\eta$ phases are formed in the MT77 (165 °C/300 min) alloy. Furthermore, Fig. 4 (f-h) also displays rod-like/thin-plate precipitates with different sizes, corresponding to $\eta'$ phase (Fig. 4(g), along $(111)_{Al}$ plane) and GPII zones (Fig. 4 (f-h)). For instance, the inserted FFT image in Fig. 4(f) shows diffraction streaks along $\{111\}_{Al}$ that corresponds to GPII zones and classical diffraction spots of $\eta'$ phase. The related IFFT images of regions 1 and 2 display obvious dislocations, but region 1 might be more stable than region 2, approaching a later stage of GPII formation. The IFFT image of region 3 (Fig. 4(f)) displays multiple stacking of alternately bright single- and double-atom layers, showing thickening along $(111)_{Al}$. The spacing between two bright single-atom layers is $d = 0.6996\ nm \approx 3d(111)_{Al} = 0.6915\ nm$, revealing a coherent $\eta'$ precipitate. Furthermore, the inserted FFT image in Fig. 4(g) shows diffraction streaks along $\{111\}_{Al}$ with multiple par-

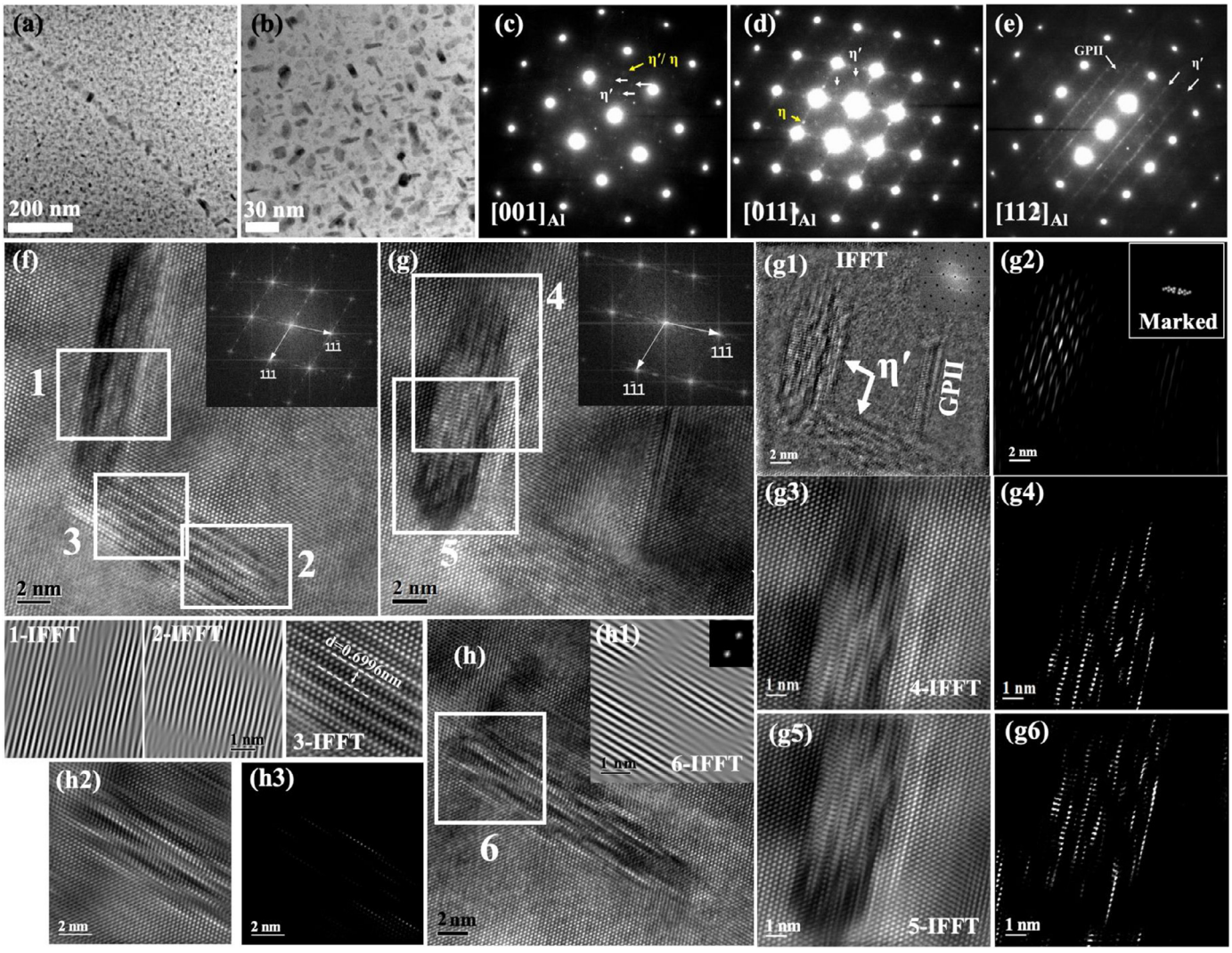


**Fig. 4.** Intragranular precipitates in the MT77 (165 °C/300 min) alloy: (a, b) TEM image, (c-e) SADE patterns, (f-h) HREM images of the precipitates. FFT images of (f, g) are inserted. (g1) IFFT images of (g) with removing Al matrix (FFT image as inserted), (g2) after adjusting image parameters (Brightness=0.43, Contrast=0.67, Gamma=0.71) of (g1) that can display bright contrast (marked FFT image as inserted). (g3) and (g5) are the IFFT images of region 4 and 5 in (g), respectively. (g4) and (g6): after adjusting brightness and gamma values of (g3) and (g5), respectively. (h1) IFFT image based on marked FFT image (as inserted) of region 6, (h2) IFFT image of region 6, (h3) after adjusting brightness and gamma values of (h2).

allel contrast, which indicates that GPII zones start to transform into $\eta'$ phase Fig. 4.(g1) shows two $\eta'$ phase particles (one with an obvious contrast), and Fig. 4(g2) clearly displays a $\eta'$ precipitate and a GPII zone Fig. 4.(g3-g6) indicates that the atomic arrangement in $\eta'$ phase is not regular and the atoms with bright contrast may equal to the simple stacking of Zn-rich layers from GPII zones Fig. 4. (h, h2) shows that the structural fluctuation containing dislocations (Fig. 4 (h1)) (the bright atoms in Fig. 4 (h3) represent Zn atom) may originate from the aggregation of multiple GPII zones. As a result, GPII zones transform firstly into $\eta'$ phase and subsequently into $\eta$ phase, i.e., $\eta_5$ or $\eta_7$ phase with an orientation relationship $(\bar{1}2\bar{1}0)\eta//(1\bar{1}\bar{1})_{Al}$[54·59]. However, some precipitates with inner structure fluctuation also exhibit similar morphology to $\eta_2$ phase with an orientation relationship $(0001)\eta_2//(1\bar{1}\bar{1})_{Al}$ and $[10\bar{1}0]\eta_2//[110]_{Al}$[54], which discloses that this phase may develop from the corresponding $\eta'$ phase with the same $\{111\}_{Al}$ habitus plane. According to the statistic precipitate sizes in Table S1 and Fig. S2, the precipitates 2.0-3.0 nm wide are GP II zones while the wider ones are $\eta'$ phase and/or possibly $\eta$ phase. As a result, it can be deduced that GP II zones can be transformed into $\eta'$ phase via thickening along $(111)_{Al}$ habitus plane (i.e., region 6 in Fig. 4(h)). Then, the complex Zn and Mg atom rearrangement will cause obvious structural fluctuation or lattice distortion inside of precipitates (i.e., region 4-5 in Fig. 4(g)), promoting GPII zones transformation to the $\eta'$ phase and then $\eta'$ to $\eta$ phase, which indicates that GPII zones would be the precursor of $\eta'$ precipitates. A structural fluctuation can complicate the diffraction spots such as the diffraction streaks along $(111)_{Al}$. Furthermore, along with atom transmission and rearrangement inside the just transformed $\eta'/\eta$ phase from GPII zones or the structurally fluctuated $\eta'$ phase, the inner ordering enables atom regularization for a more stable state. This might be one transformation mechanism from metastable GP zones to more stable configurations such as $\eta'$ phase.

With increasing retrogression temperature to 175 °C and holding for 300 min (MT77 (175 °C/300 min)), the intragranular precipitates are obviously grown along with granular precipitates (4.0-12.0 nm) (Fig. 5 (a-c), also see Table S1 and Fig. S2) Fig. 5. (d-f) displays the diffraction spots of $\eta'$ phase that are partially overlapped with those of $\eta$ phase (yellow-marked in Fig. 5(d)), as well as weak diffraction spots of GPII zones (Fig. 5(f)). The FFT image of Fig. 5(g) exhibits diffraction spots of $\eta'$ phase with orientation relationship of $\{10\bar{1}0\}_{\eta'}//\{\bar{2}20\}_{Al}$, and Fig. 5 (g1) shows that the Zn-

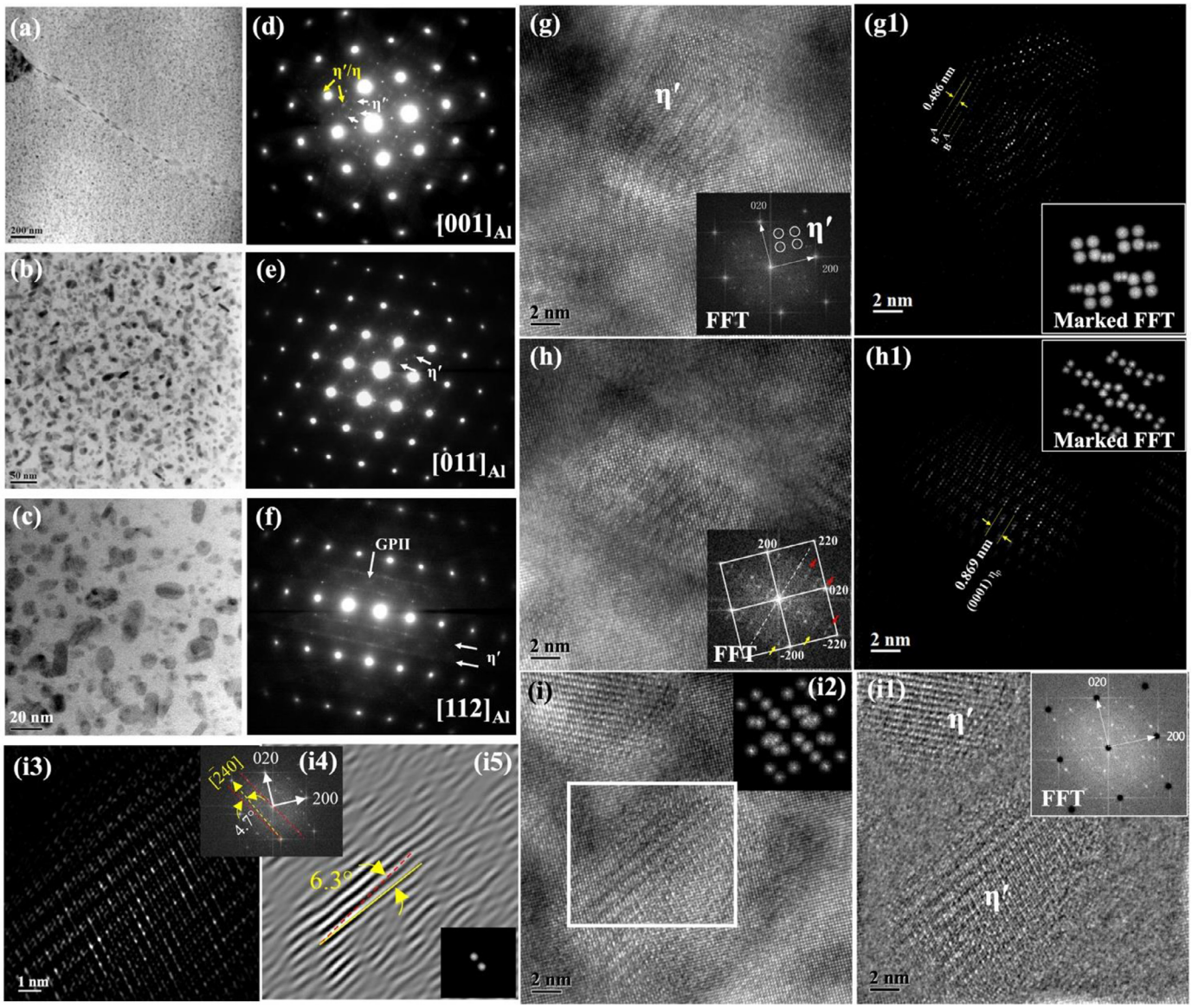


**Fig. 5.** TEM (a-c), SADE patterns (d-f) and HREM (g-i) images of the MT77 (175 °C/300 min) alloy. (g1) IFFT image of (g, FFT image as inserted) after adjusting image parameters (Brightness=0.47, Contrast=0.67, Gamma=0.69), (h1) IFFT image of (h, FFT image as inserted) after adjusting image parameters (Brightness=0.43, Contrast=0.65, Gamma=0.69), (i1) IFFT images of (i) with removing Al matrix (FFT image as inserted), (i2) marked FFT image of FFT image in (i4) from the white region in (i), (i3) IFFT image from (i2), (i5) IFFT image from the marked FFT image (as inserted) along $[\bar{2}40]_{Al}$ direction.

rich layers are arranged as ABAB type along the *a* axis with an interplanar spacing of 0.486 nm. Then, Fig. 5(h) shows a precursor $\eta_p$ ($P6_3/mmc$, $a = 0.496$nm, $c = 0.869$nm) for $\eta$ phase[60] featuring complex diffraction spots with diffraction streaks along $\{220\}_{Al}$ direction in an FFT image (Fig. 5(h)) including that of $\eta'$ phase ($1/3\{022\}_{Al}$ and $2/3\{022\}_{Al}$, as yellow-marked) and others as red-marked, similar to those of $\eta_1$ phase with a long and fully coherent interface with Al matrix[53]. The IFFT image in Fig. 5 (h1) exhibits Zn atoms with similar position in line with *c* axis but stacked as ABAB type perpendicular to *c* axis Fig. 5. (i, i1) shows two $\eta'$ precipitates: one with major axis along $[420]_{Al}$ while the other with major axis along $[4\bar{2}0]_{Al}$, both demonstrating a specific orientation relationship with $\{\bar{2}40\}_{Al}$ Fig. 5. (i4) indicates there is a 4.7° misorientation of $\eta'$ phase relative to that stacked along $\{\bar{2}40\}_{Al}$, which might be strained by the rearrangement of vacancies and atoms, or be difficult to distinguish from partial diffraction spots after FFT processing due to noise. However, it reveals that this $\eta'$ phase is immature like a precursor. After IFFT processing with the closest diffraction spots along $[\bar{2}40]_{Al}$ yellow-arrowed in Fig. 5 (i4), it is found that there is a 6.3° misorientation between the fringe and $(\bar{2}40)_{Al}$ plane with a fringe spacing of 0.872 nm. Thus, the MT77 (175°C/300 min) alloy mainly contains $\eta'$ and some $\eta$ precipitates with lesser number of GPII zones.

*3.3.1.3. MT77 processes with retrogression at 160/165/175 °C for 600 min.* With prolonging retrogression time to 600 min at 160 °C in the MT77 process, coarse (as marked in Fig. 6(b)) and fine (<5 nm) intragranular precipitates (Fig. 6(a)) are formed densely with a needle-like morphology (Fig. 6(c)) (see sizes in Table S1 and Fig. S2), while some spherical particles (~10 nm) may be the cross sections of these needle-like precipitates Fig. 6. (d-f) mark the typical diffraction spots of $\eta/\eta'$ phase and GPII zones, and the coarse rod-like precipitates marked in Fig. 6 (b, c) may represent the $\eta$ phase while the needle-like and some spherical ones are e $\eta'$ phase, as well as finer ones corresponding to GPII zones or the $\eta'$ phase Fig. 6.(g) shows two precipitates: one (region 1) is stacked along

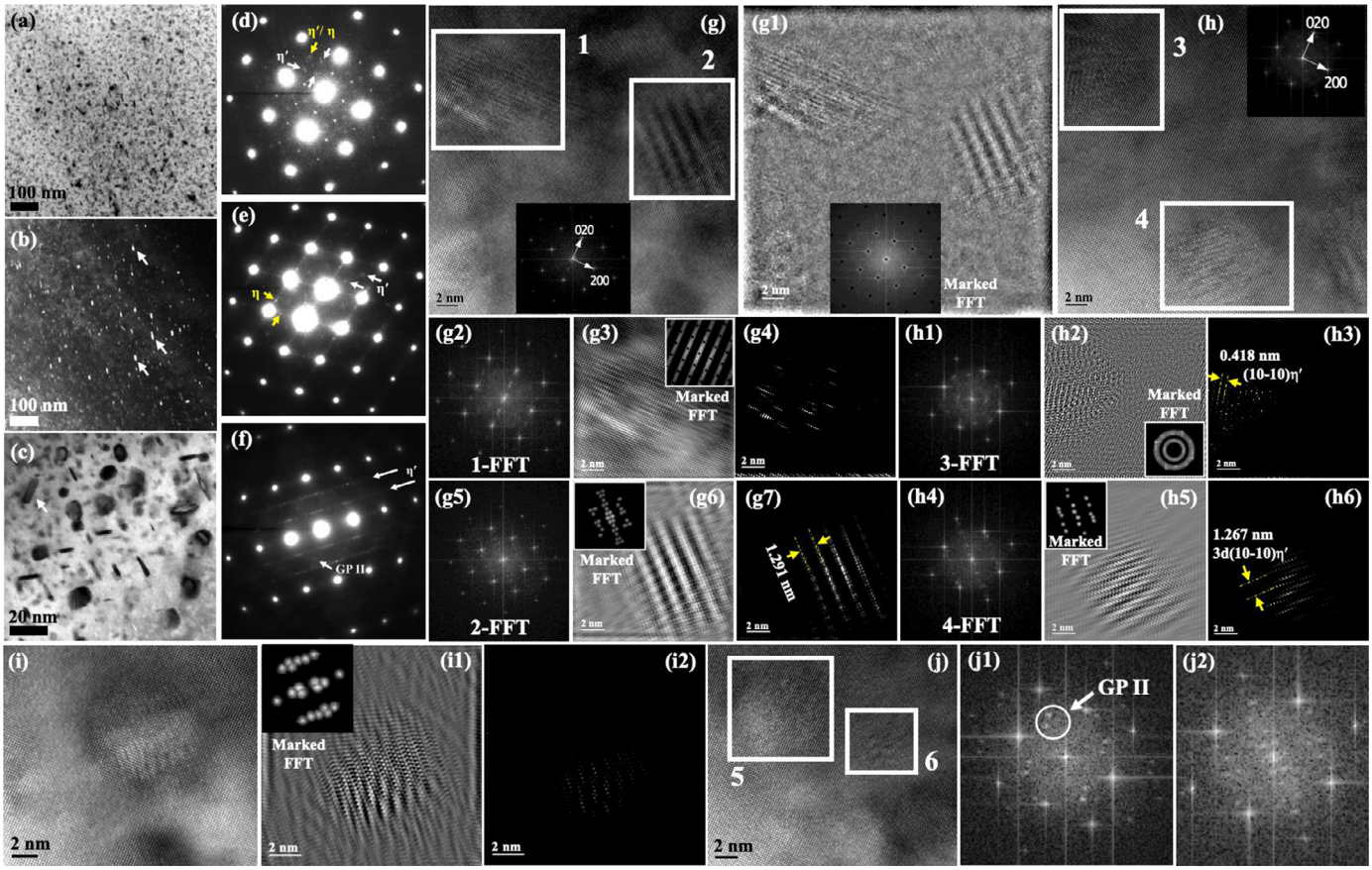


**Fig. 6.** TEM (a-c, a: bright field, b: dark field) and HREM (g-j) images of the MT77 (160 °C/600 min) alloy. (d-f) SADE patterns, (g1) IFFT images of (g, FFT image as inserted) with removing Al matrix, (g2, g5, h1, h4) FFT images of regions 1-4 in (g, h), (g3, g6, h2, h5) IFFT images of regions 1-4 in (g, h) (marked FFT images as inserted), (g4, g7, h3, h6) IFFT image of regions 1-4 in (g, h) after adjusting image parameters (Brightness=0.47, Contrast=0.66, Gamma=0.68). (i1) IFFT images of the precipitate in (i, FFT image as inserted), (i2) IFFT image after adjusting image parameters of (i1), (j1) and (j2) are the FFT images of regions 5 and 6 in (j), respectively.

$(020)_{Al}$ and almost coherent with the Al matrix with partial atom rearrangement. Previous studies[53·54] indicated that $\eta_1$ and $\eta_9$ phases possess an orientation relationship with $\{020\}_{Al}$, hence, this precipitate may be growing as a precursor of $\eta_1$ and $\eta_9$ phases. The other one stacked along $(\bar{2}20)_{Al}$ can be a precursor of $\eta$ phase with close packing of atoms along $(0001)\eta$ but those are not well distinguished in the IFFT image in Fig. 6 (g7). The FFT image of region 3 in Fig. 6(h) shows vague diffraction spots along $(\bar{4}20)_{Al}$, and its IFFT image in Fig. 6 (h2, h3) based on the bright spots in Fig. 6 (h1) displays lamellar stacking with a spacing of 0.418 nm that may correspond to $(10\bar{1}0)_{\eta'}$. Region 4 in Fig. 6(h) exhibits a different orientation compared to region 3, i.e., diffraction spots along $(\bar{2}20)_{Al}$, which could be a precursor of $\eta'$ phase. The FFT image in Fig. 6(i) is similar to Fig. 6 (j2) but different from Fig. 6 (j1) that shows diffraction spots of GP II zone, and Fig. 6 (i2) exhibits close stacking of bright Zn atoms, which along with Fig. 6 (g4) demonstrates that this precipitate may be a precursor of $\eta$ phase. As a result, the MT77 (160 °C/600 min) alloy contains metastable $\eta'$ phase, GPII zones and $\eta$ phase or a precursor of $\eta$ phase.

After retrogression at 165 °C for 600 min, uniform precipitates (Fig. 7 (a, b)) alongside some larger ones (as marked in Fig. 7(b)) are obtained in the MT77 (165 °C/600 min) alloy (see sizes in Table S1 and Fig. S1). Similarly, abundant spherical precipitates (<10 nm and partial <5 nm) and a few coarse rod-like precipitates coexist (Fig. 7(c)). The typical diffraction spots or streaks of $\eta/\eta'$ phase and GPII zones are marked in Fig. 7 (d-f)) Fig. 7.(g) shows a rod-like precipitate with the long axis parallel to $[210]_{Al}$ growing along $(\bar{2}40)_{Al}$ plane. With adjusting the brightness and contrast of the corresponding IFFT image (bottom white region in Fig. 7(g)), multi-layer stacking is revealed. Its diffraction spots along $(\bar{2}20)_{Al}$ in FFT image are not aligned but rather regularly off-positioned, indicating a regular structural fluctuation in this rod-like precipitate, which may be a modulated structure towards $\eta$ phase. Meanwhile the FFT image of the upper white region in Fig. 7(g) with obvious contrast exhibits diffraction spots of a GP zone. Moreover, the FFT/IFFT images of the precipitate in Fig. 7(h) show the semi-coherent $\eta'$ phase with $(10\bar{1}0)_{\eta'}//(\bar{2}20)_{Al}$ relationship and $d(10\bar{1}0)_{\eta'} = 3d(\bar{2}20)_{Al}$. These observations reveal that the MT77 (165 °C/600 min) alloy contains metastable $\eta'$ phase, GPII zones and $\eta$ phase, the last one is represented by coarse precipitates marked in Fig. 7(b).

After MT77 (175 °C/600 min) treatment, homogeneously distributed intragranular precipitates including rod-like ones are formed (Fig. 8 (a, b), see sizes in Table S1 and Fig. S2). There are fewer fine spherical precipitates although some with size <10 nm and flaky/needle-like ones still appear (Fig. 8(b)). The typical diffraction spots or streaks of $\eta/\eta'$ phase and GPII zones (Fig. 8 (c-e)) can be observed, which is supported by the HRTEM results in Fig. 8 (f-h) Fig. 8.(f4) shows diffraction spots near $1/2\{02\bar{2}\}_{Al}$ and $1/2\{200\}_{Al}$ (severe noise), and Fig. 8 (f5) clearly shows layered features after the rearrangement of vacancies and atoms. These observations indicate that region 2 in Fig. 8(f) may correspond to the precursor $\eta_p$ phase ($P6_3/mmc$, $a$ = 0.496 nm, $c$ = 0.869 nm)[60], rearranged along $(02\bar{2})_{Al}$ and similar to that shown in Fig. 5 (h, h1). An irregular precipitate in Fig. 8(g) is similar to $\eta_{12}$ phase with the orientation relationship $(0001)\eta_{12}//(31\bar{1})_{Al}$, $[11\bar{2}0]\eta_{12}//[110]_{Al}$[59],

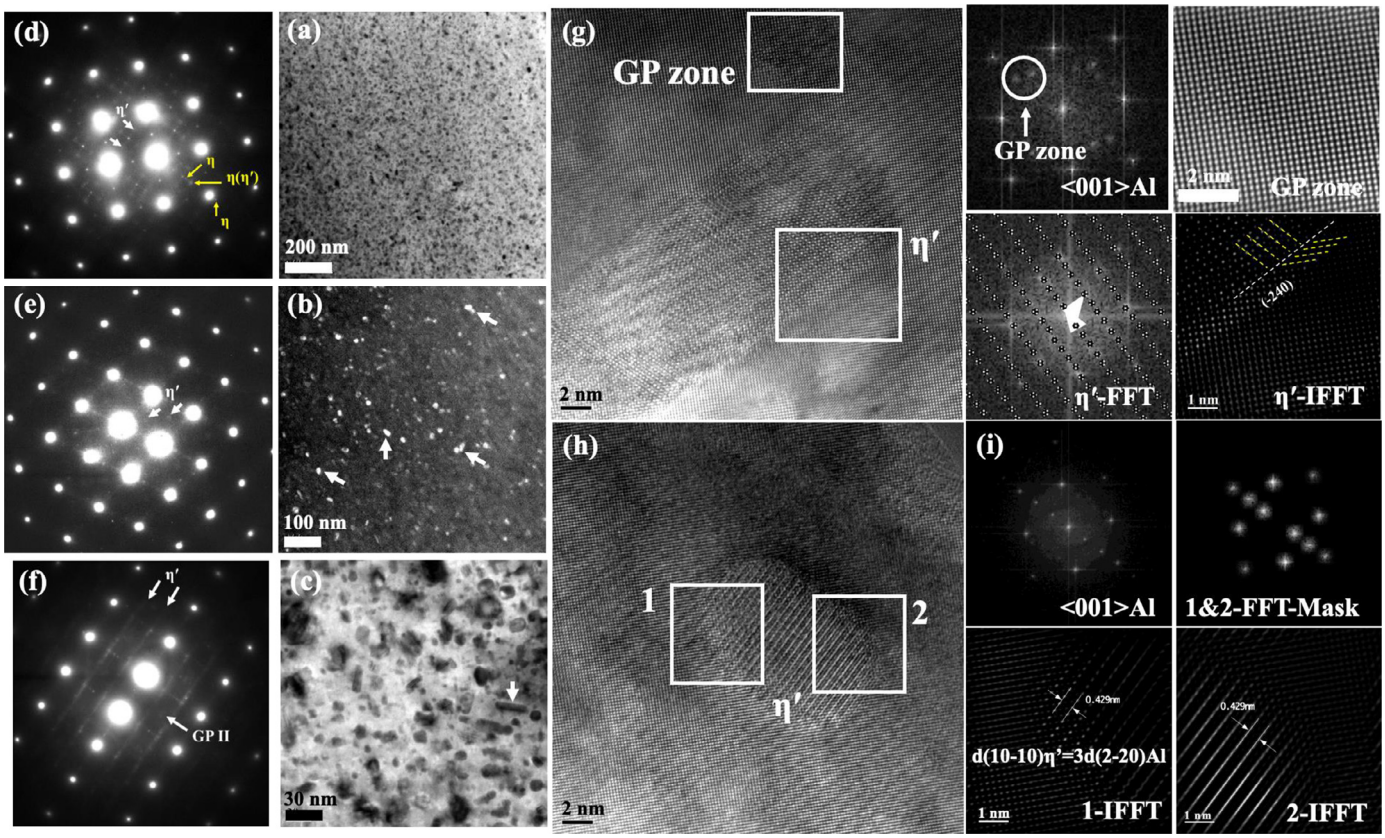


**Fig. 7.** TEM (a-d, b is dark-field image) and HREM (g, j) images of the MT77 (165 °C/600 min) alloy. (d, e, f) SADE patterns. The FFT and IFFT images of upper and bottom white regions in (g) are shown at right; (i) FFT image of (h); the FFT and IFFT images of regions 1 and 2 are shown at right.

and contains an obvious domain boundary and a stacking fault as well as a stacking layer of ABC type (Fig. 8 (g2, g3)), which is gradually grown into $\eta_{12}$ phase with $(0001)_{\eta 12}$ layer. This signifies that this phase is formed as a transformational precursor and supports the orientation relationship $(0001)_{\eta 12}//(31\bar{1})_{Al}$, which means that $\eta_{12}$ phase is grown via rearrangement of vacancies and atoms along $(31\bar{1})_{Al}$. For its immature state with domain and stacking faults, there are many satellite-like patterns in the FFT image (inset in Fig. 8(g)). Moreover, Fig. 8(h) shows another $\eta_{12}$ phase with the same orientation relationship to that in Fig. 8(g) but this $\eta_{12}$ phase is developed to a full-grown state with noticeable $\eta'$ structure near its edge, indicating that $\eta_{12}$ phase is grown by consuming adjacent $\eta'$ phase. Additionally, Fig. 8 (i, j) shows two precipitates with obvious structural fluctuation that represents localized lattice distortion. Their SAED patterns (Fig. 8(i1, ji)) exhibit complex diffraction spots/streaks along $(111)_{Al}$ and weak diffraction spots of $\eta'$ phase. Their morphologies are similar to those reported in a previous study that shows diffraction features of $\eta$ or $\eta'$ phase[54].

It is known that the diffraction streaks along $(111)_{Al}$ are closely related with GPII zones[54], however, Fig. 8 (i1, j1) exhibits dense diffraction spots along $(111)_{Al}$, which demonstrates that these two precipitates may be composed by multiple GPII zones or are being formed via the growth of GPII zones by further absorbing adjacent GPII zones as marked in Fig. 8(i). They are identified as $\eta'$ phase that is transformed from GPII zones and grown/thicken along $\{111\}_{Al}$ planes - the habitus plane of $\eta'$ phase. Therefore, $\eta'$ and $\eta$ phases as well as GP II zones are formed in the MT77 (175 °C/600 min) alloy, and the coarse particles in Fig. 8(b) could be either $\eta$ or a larger $\eta'$ precipitate. With extending retrogression time at 175 °C to 900 min, more coarse precipitates appear along finer ones (< 5 nm) (Fig. 9 (a, b)). Likewise, Fig. 9 (c, d) demonstrates the appearance of $\eta'$ and $\eta$ phases. As a result, the coarser precipitates in Fig. 9(b) are $\eta$ phase while spherical and finer ones are $\eta'$ phase or possible GPII zones (weak diffraction spots appear in 1/2[311] position in Fig. 9(d)). Compared to T6 state, the MT77 (175 °C/900 min) treatment causes obvious growth/coarsening of intragranular precipitates mostly in $\eta$ phase, subsequently bringing down the precipitation hardening ability or strength, whereas it can distinctly increase the electrical conductivity.

### 3.3.2. Precipitates along grain boundaries

Hot-rolled high-strength Al alloy plates are usually composed of recrystallized and unrecrystallized grains that can affect local solute distribution and precipitation, especially near GBs[11,61-63] Fig. 10. shows that in T6 state the subgrain/substructure boundaries are decorated with continuous GBPs with not well defined PFZs. With T77 (200 °C/5 min) treatment, the GPBs are discretely distributed with visible PFZs (Fig. 10 and Table S1). Prolonging retrogression time to 40 min (T77 process) leads to GBPs coarsening and wider PFZs (Fig. 10 and Table S1), besides some fine precipitates with size < 20 nm near GBs. With decreasing retrogression temperature, the coarse and discontinuous GBPs are also observed with PFZs (Fig. 10), while fine GBPs and less-pronounced PFZ (white-marked in Fig. 10) are found along subgrain boundaries. In general, the GBPs sizes and PFZ widths are increased with retrogression temperature and time, especially with MT77 (175 °C/(600-900) min) treatment causing coarser GBPs and wider PFZs (Fig. 10 and Fig. 9(a), Table S1 and Fig. S2). Table S1 indicates that the intragranular precipitates in the MT77 (155 °C/300 min), MT77 (165 °C/300 min) and MT77 (160 °C/600 min) alloys (with few $\eta$ precipitates) become larger than those in the T6 state. Further increasing the retrogression time or temperature enhances the coarsening of precipitates and induces a possible phase transformation (GP zone to $\eta'$ phase and/or $\eta'$ to $\eta$ phase). This alleviates the pre-

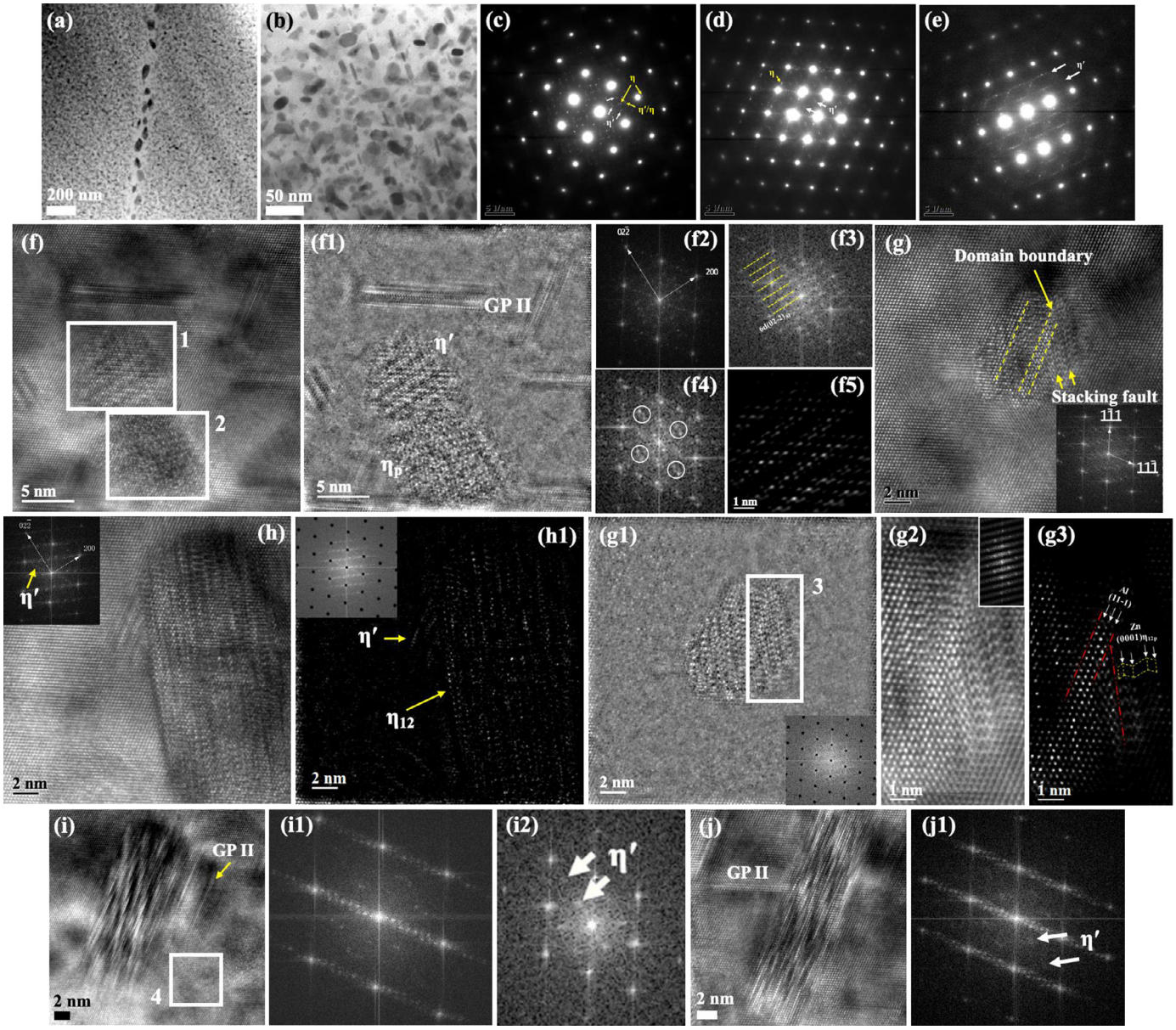


**Fig. 8.** TEM (a, b), SADE (c-e) patterns and HREM (f-j) images of the MT77 (175 °C/600 min) alloy. (f1) IFFT images of (f) with removing Al matrix (FFT image in (f2)), (f3) and (f4) are the FFT image of regions 2 and 1 in (f), respectively. (f5) IFFT image of (f4) (Brightness=0.49, Contrast=0.67, Gamma=0.64). (g1) IFFT images of (g) with removing Al matrix (FFT image as inserted in (g)), (g2) IFFT image of region 3 in (g1) (FFT image as inserted), (g3) IFFT image of region 3 in (g1) after adjusting image parameters (Brightness=0.42, Contrast=0.56, Gamma=0.68). (h1) IFFT image of (h, FFT image as inserted) after adjusting image parameters (marked FFT image as inserted in (h1). (i1) and (j1) are FFT images of (i) and (j), respectively. (i2) FFT image of region 4 in (i).

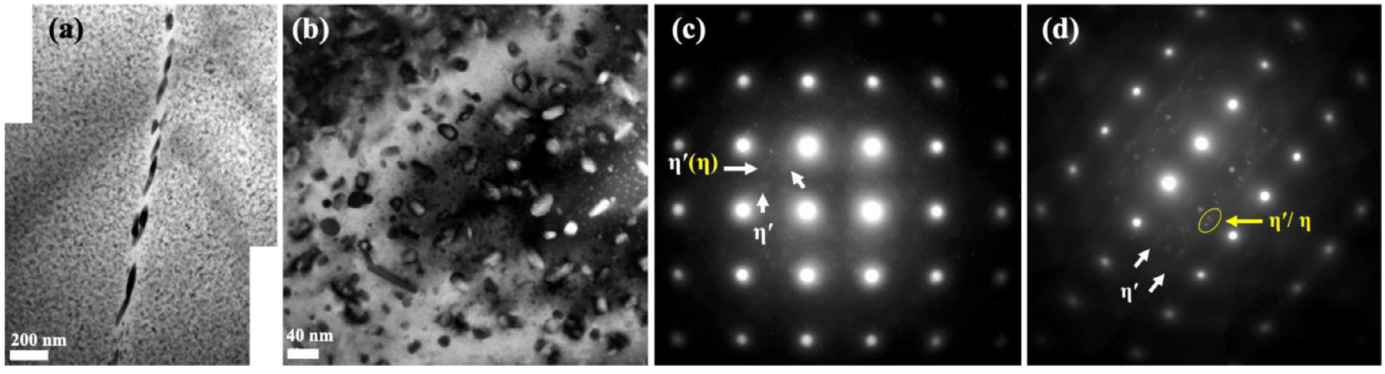


**Fig. 9.** TEM (a, b) images and SADE patterns along $[001]_{Al}$ (c) and $[112]_{Al}$ (d) zone axis of the MT77 (175 °C/900 min) alloy.

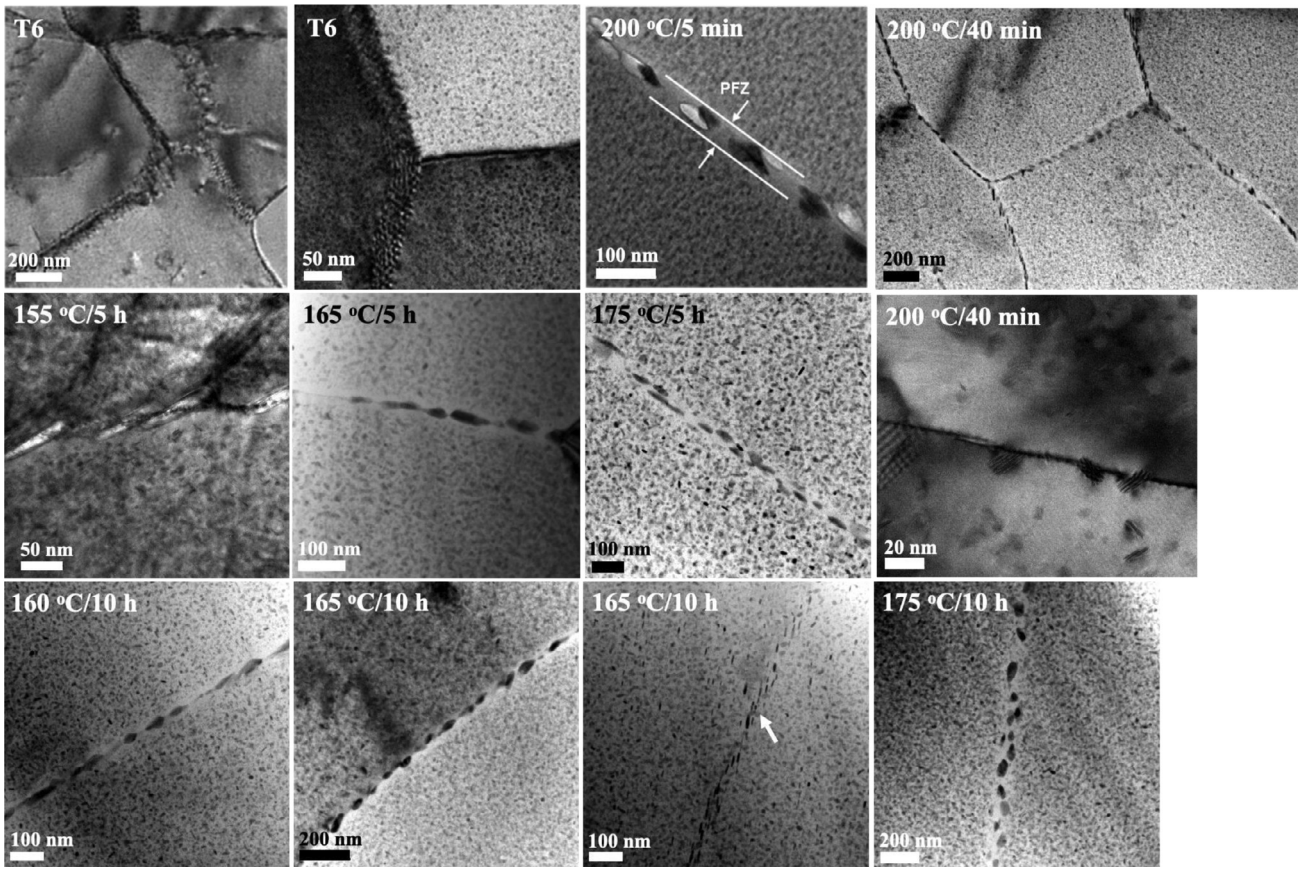


**Fig. 10.** GPBs and PFZs near GBs in the T6-, T77- and MT77-treated alloys. A high magnification GB image of MT77 (200 °C/40 min) alloy and GBPs possibly along high angle grain boundaries (HAGBs) of MT77 (165 °C/600 min) alloy are shown.

cipitation strengthening potentials and decrease the strength (see Fig. 1), especially in case of the formation of more $\eta$ precipitates.

### 3.4. Optimal MT77 process for an 86-mm thick plate

From Sections 3.1 and 3.2, both MT77 regimes, i.e. 160 °C/900 min and 165 °C/600 min are suggested for their better combination of strength and electrical conductivity. With taking it into account that it is much easier to control time than temperature, the MT77 (165 °C/600 min) process is preferred for its relatively short retrogression time. When it was applied to an ~86-mm thick AA7050 Al alloy plate, an almost uniform through-thickness YS/UTS were obtained, except for slightly higher values near surface (Fig. 11), similar to the change of microhardness. Note that the different level of properties as compared to those given before reflects different alloying levels, with both YS and UTS being higher than the minimum LT strength of 7050-T7651 plate (51-76 mm) (UTS $\geq$ 524 MPa, YS $\geq$ 455 MPa)[64]. The electrical conductivity is above 38% IACS at the center and lesser near the surface, which indicates that a higher strength corresponds to a lower electrical conductivity, in line with that in Fig. 1 Fig. 12. shows uniformly distributed intragranular precipitates ($<$ 17 nm) in the surface and center layers along with discrete GBPs: 50-95 nm length and 15-35 nm width in the surface layer (PFZ width: 35-55 nm), and 50-80 nm length and 10-20 nm width in the center layer (PFZ width: 30-50 nm). The SAED patterns reveal that both $\eta'$ and $\eta$ phases appear in the surface/center layer, e.g., a coarse $\eta$ precipitate (size: ~20 nm, Fig. 12(k)) and a fine $\eta'$ precipitate or a GP zone ($<$ 10 nm) in Fig. 12 (k, m). This coarse precipitate in Fig. 12(k) may represent $\eta_{12}$ phase with an orientation relationship $(0001)\eta_{12}//(31\bar{1})_{Al}$ and $[2\bar{1}\bar{1}1]\eta_{12}//[110]_{Al}$, different from previously reported $[11\bar{2}0]\eta_{12}//[110]_{Al}$, which requires further examination. In view of the variation of properties along the plate thickness, it can be deduced that, in comparison with the precipitates in the surface layer, the relatively larger precipitates along with a greater amount of $\eta$ phase in the central layer can raise electrical conductivity but reduce strength, in line with the properties in Fig. 11. The temperature gradient along the plate thickness during solution, quenching and aging treatments may be also responsible for these differences. High cooling rate and enough holding time at aging temperature near the surface layer can promote rapid nucleation and high-number density precipitates. But insufficient holding time at solution/aging temperature and relatively low cooling rate near the central layer could cause more precipitates (i.e., the stable $\eta$ phase) during quenching and low solubility in the matrix that will diminish subsequent precipitation during MT77 treatment. Thus, the through-thickness quenching/cooling rates or temperature gradients should be alleviated or improved via increasing quenching/cooling rates or designing alloys with a low quenching sensitivity.

### 3.5. Correlating precipitate evolution with properties of the T77 and MT77 alloys

The above studies indicate that the dominant GP zones and $\eta'$ phase in the MT77 (155 °C/300 min) alloy, similar to those in T6 state with comparable strength (Fig. 1), are changed into mainly $\eta'$ phase and GPII zones along with some $\eta$ precipitates in the MT77 (165 °C/300 min) alloy, which are further replaced by dominant $\eta'$ and some $\eta$ (or precursors of $\eta$ phase) precipitates in

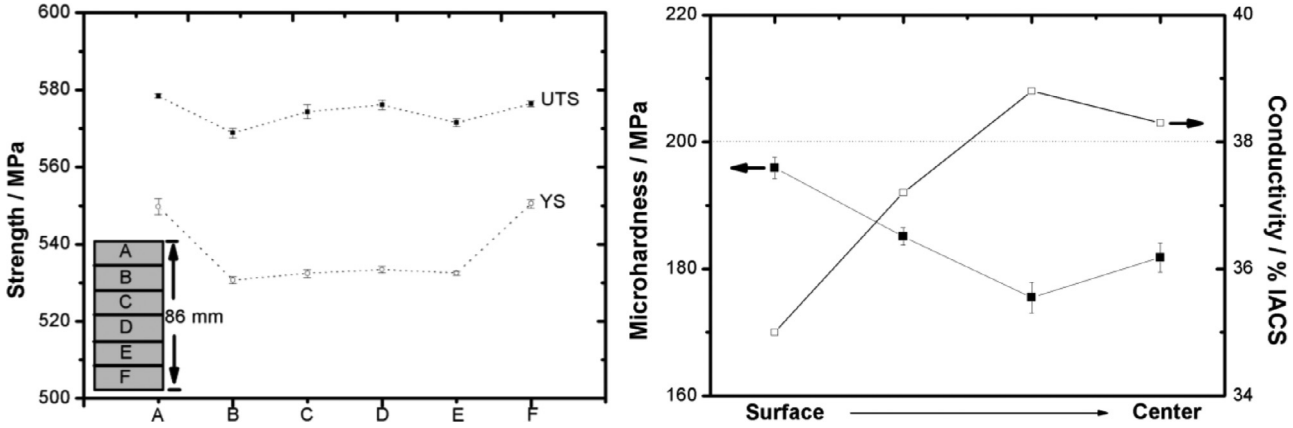


**Fig. 11.** The properties along the thickness of the MT77 (165 °C/600 min) treated 7050 Al alloy plate.

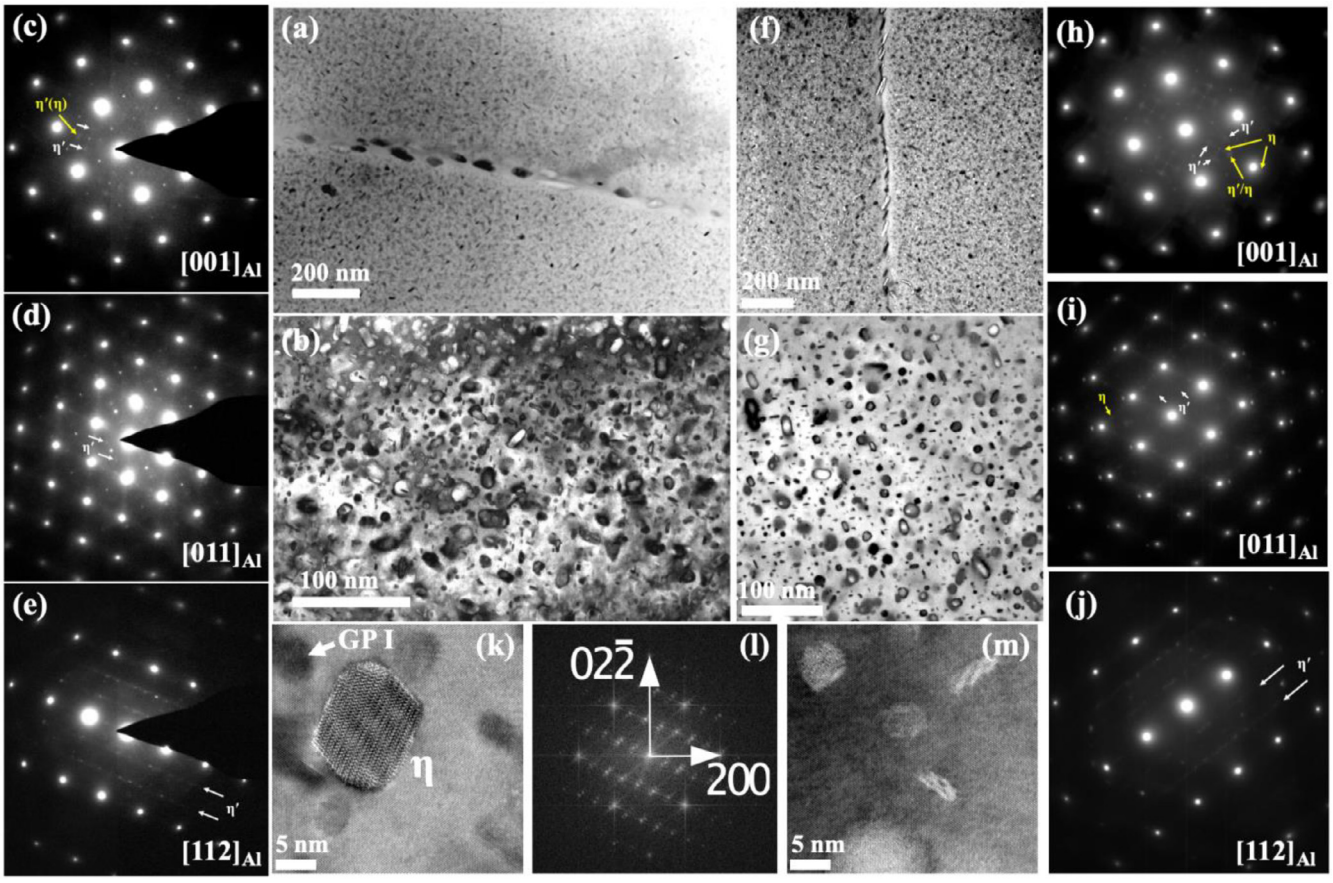


**Fig. 12.** Intragranular and intergranular precipitates (a, b, f, g) and SAED patterns (c-e, h-j) near the plate surface (a-e) and center (f-m) of the MT77-treated 7050 Al alloy plate. (k, m) HREM images, (l) FFT image of coarse precipitate in (k).

the MT77 (175 °C/300 min) alloy. This demonstrates that increasing the retrogression temperature in the MT77 process can promote the growth of (metastable) precipitates and the transformation into succeeding stable ones, and even result in formation of coarse, stable $\eta$ precipitates. According to the selection of precipitates after different single-step aging regimes of Al-Zn-Mg-Cu series alloys, as schematically shown in Fig. 13, it can be found that GPI/II zones forming at low aging temperature (i.e., below blue line) can be transformed into the metastable $\eta'$ phase (i.e., between yellow and blue lines) with increasing aging temperature or time, and further into stable $\eta$ phase at higher aging temperature or longer aging time (as shown in the inset). For example, after room-temperature aging for ~3 years, $\eta'$ phase and GPI/II zones coexist, and stable $\eta$ phase is dominant after aging at ~150 °C for 6000 min[65·66]. However, it also shows that GP zones and $\eta'$ phase can be dissolved below ~150 °C and above ~220 °C, respectively. Thus, with retrogression at 200 °C after peak aging (i.e., 120 °C/1440 min), considerable number of $\eta'$ phase and GP zones can be dissolved into matrix with short retrogression time (for relatively thin plates/sheets) so as to increase the matrix solute and vacancy concentrations (these vacancies (or quenching vacancies) were trapped in these precipitates during T6 aging). At the same

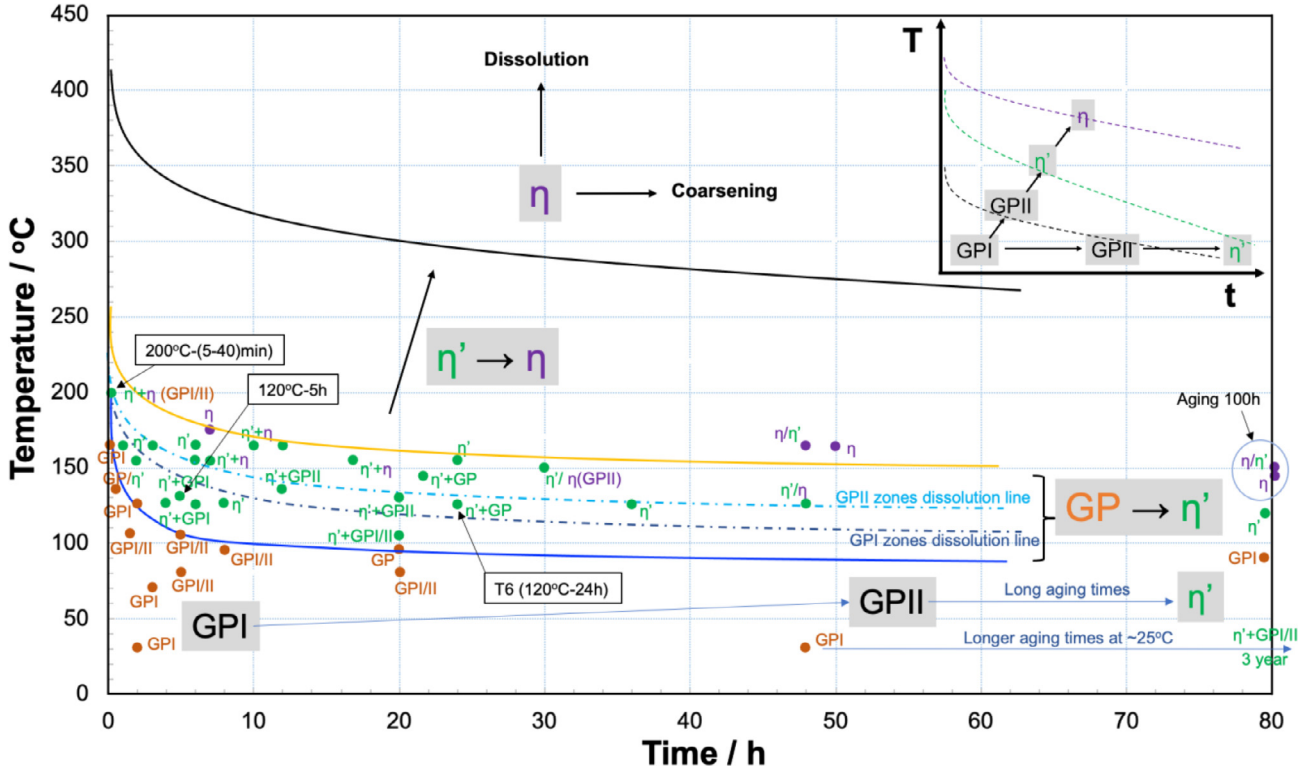


**Fig. 13.** Temperature-time transformation of precipitates in Al-Zn-Mg-(Cu) 7XXX-series alloys (single-step aging data are collected from published data) (the inset shows the possible transformation sequence with changing temperatures and times according to ref.[67]).

time, this drives the growth and/or transformation of larger precipitates with critical sizes into more stable ones such as $\eta'$ or even $\eta$ phase, that will be further coarsened or transformed during the third-step aging (i.e., 120 °C/1440 min) such as via ripening process. As a result, the mechanical properties are obviously decreased along with increased electrical conductivity (Fig. 1). This signifies that noticeable precipitate growth and formation of $\eta$ phase during retrogression at 200 °C in the T77 processing can highly affect the solute concentration in the matrix and the final aging strengthening. Lowering retrogression temperature equals to thermodynamically and/or kinematically delay/suppression of the transformation from metastable GP zones/$\eta'$ phase into stable ones at longer retrogression time, while promoting the dissolution of smaller/fine precipitates for final re-aging hardening. As supported by MT77 process with low retrogression temperature (for 300 min), a higher strength is obtained in comparison with that of T77 alloy (as shown in Fig. 1), and the corresponding longer retrogression time can ensure a controllable RRA process for (mid-)thick plates. Meanwhile, the formation of more complex phases (i.e., $\eta'$ phase and GPII zones) in the MT77 alloy (i.e., retrogressed for 300 min) may help increase electrical conductivity (Fig. 1) but it remains lower than that of the T77 alloy (i.e., retrogressed at 200 °C/40 min), because the formation of numerous coarser $\eta/\eta'$ precipitates (as shown in Fig. 2) can relax the matrix lattice distortion (as stated in section 3.2). With retrogression at 160-175 °C for 600 min, GPII zones, $\eta'$ and $\eta$ phases are gradually replaced by the dominant $\eta'$ and $\eta$ (or precursor of $\eta$ phase) phases along with increased precipitate sizes (Figs. 6-8 and Table S1). These changes in the precipitation processes explain why, as shown in Fig. 1, the MT77 (165°C/(600-900 min) regime results in a lower strength than that of T6 state. For the suggested MT77 (165 °C/600 min) treatment in Section 3.2, it can be determined that $\eta'$ phase and GP II zones are dominant along with few ineluctable $\eta$ precipitates, without obvious growth or coarsening of intragranular precipitates. This can ensure the qualifying of electrical conductivity (≥ 38% IACS) with less strength loss, i.e., 4.6% (YS) and 7.0% (UTS) reduction compared to T6 state, which can be further reduced to 2.5% (YS) and 5.6% (UTS) with the MT77 (160 °C/900 min) treatment (the percentages are calculated based on the data in Fig. 1).

The aforementioned analysis clearly indicates that the metastable precipitates (i.e., GP zones or $\eta'$ phase in T6 state) can be gradually replaced by $\eta'$ and/or $\eta$ phases after the T77 or MT77 treatment, thus increasing the electrical conductivity, which correlates with a better corrosion resistance[43–46] relative to that of the T6 state (Fig. 1). Fig. S3 clearly shows that the intergranular corrosion depth of the MT77-treated alloy is close to the T77-treated one but obviously smaller than that of T6 state. However, the T77 process with retrogression at 200 °C decreases the strength noticeably (as shown in Fig. 1) while efficiently increasing electrical conductivity, and the rapid responsiveness to retrogression at 200 °C is difficult to control for (mid-)thick plates because of insufficient heat input or retrogression towards plate center. Otherwise, $\eta'$ phase or GP zones with critical sizes after T6 aging[68·69] may quickly grow and/or transform into $\eta$ and/or larger $\eta'$ precipitates during retrogression at or above 200 °C. Following the third-step aging, the increased number and sizes of precipitates can relax lattice distortion/stress and increase electrical conductivity. Thus, the T77 (200 °C/40 min) alloy with relatively coarse intragranular and intergranular precipitates (Table S1) exhibits more sufficient intragranular precipitation and growth of GBPs and PFZs, corresponding to more relaxed lattice distortion compared to that of the MT77 treated alloys, which still exhibit obviously improved corrosion resistance compared to that of T6 state along with higher mechanical properties than those of the T77 (200 °C/40 min) alloy. This reveals that the first-step aging is particularly important for subsequent precipitation manipulation. In this study, with using 120 °C/300 min as the first-step aging process, high-number density needle-like / granular precipitates

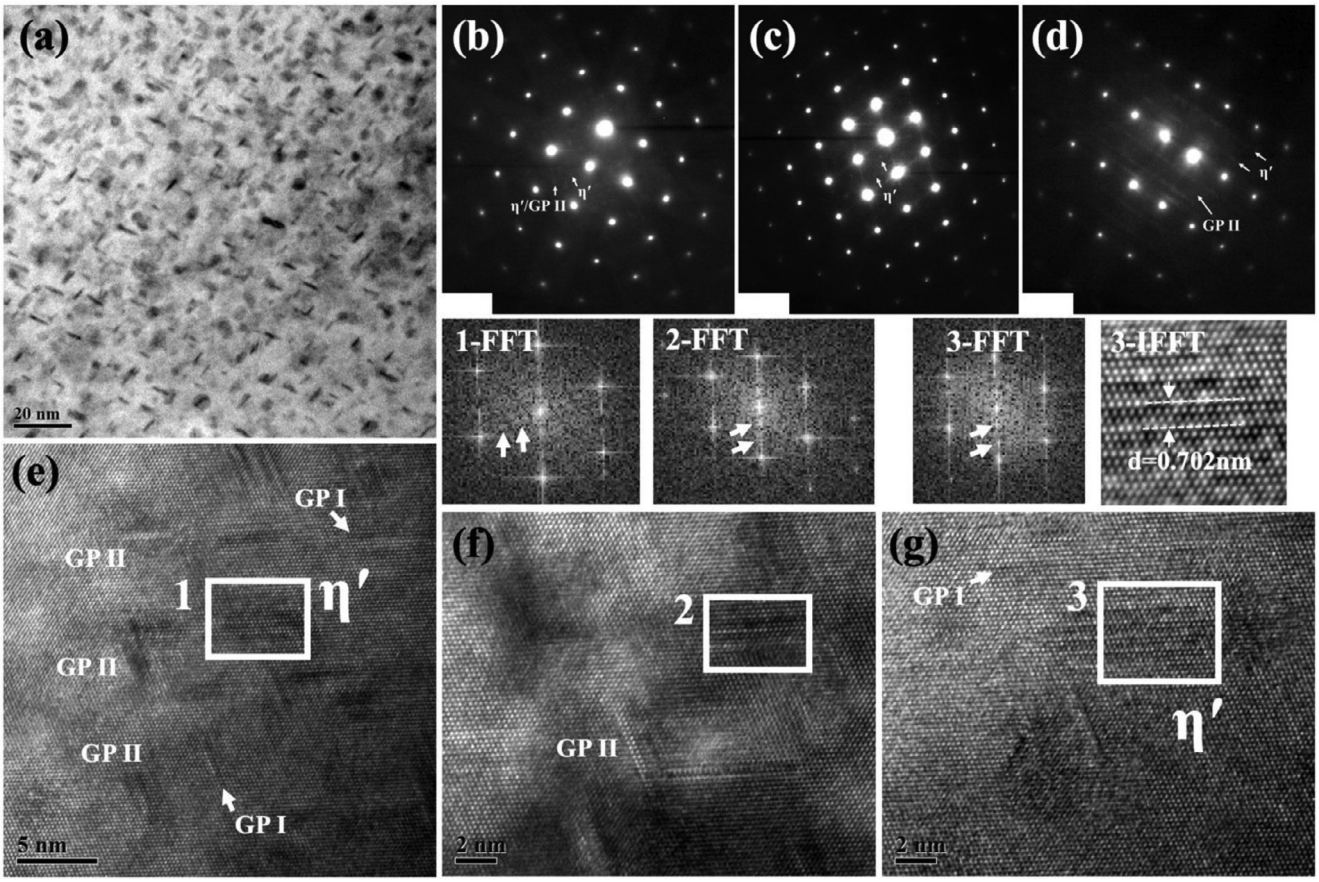


**Fig. 14.** TEM (a), SADE (b-d) patterns and HREM (e-g) images of the 120 °C/300 min aged alloy. The FFT or IFFT images of region 1-3 are marked with corresponding numbers.

(length < 8 nm and width < 3 nm, see Figs. 14 and S4) are formed along $\{111\}_{Al}$ and some exhibit obvious alternate single-layer and double-layer atom stacking, i. e., regions 1-3, similar to region 3 in Fig. 4. Both diffraction spots and HREM images indicate these precipitates are mainly coherent GPII zones and $\eta'$ phase as well as GPI zones (atom clusters). Region 2 in Fig. 14(f)) shows two alternate single-layer and double-layer atom stackings and region 3 shows 2-3 developing alternate single-layer and double-layer atom stackings while region 3 shows multiple alternate atom stacking with the spacing of two bright atom layers $d$=0.702 nm, similar to that of region 3 in Fig. 4. This indicates that disc-like GPI and GPII zones can be easily formed during aging at 120 °C and thickened along $\{111\}_{Al}$ from about 1-2 atom layers to 4-6 atom layers, forming alternate stacking structures (i.e., $\eta'$ precipitate in Fig. 14 (e-g)) whose growth/thickening might be promoted by adjacent GPI and GPII zones. This is in line with the precipitation sequence proposed by Berg et al [55].: SSS (supersaturated solid solution) → VRC (vacancy-rich clusters) → GPII → $\eta'$ → $\eta$. However, the number and sizes of intragranular precipitates such as GP zones and $\eta'$ phase as well as GBPs after 120 °C/300 min aging should be significantly fewer/smaller than those of the T6 (120 °C/1440 min) state. Combined with lower retrogression temperature, the phase transformation and growth / coarsening of $\eta'$ and/or $\eta$ phases can be postponed along with controlled dissolution of intragranular precipitates, which can ensure a relatively high solute concentration in Al matrix for the third-step aging strengthening.

Additionally, based on the schematic connection of different factors affecting the properties of high-strength Al alloys, as shown in Fig. 15, severe corrosion damage such as IGC/SCC (a key bottleneck for T6 treated alloys) is highly correlated with continuously distributed GBPs, usually causing continuous corrosion path along GBs[9·37·52] and enabling intergranular cracking/fracture. As effective sinks for dislocations and vacancies, GBs can accelerate solute diffusion, absorb solutes/vacancies and facilitate the formation of GBPs along with appearance of PFZs[70], which can, in addition to coarse insoluble particles, determine both strength/fracture and corrosion resistance, as shown schematically in Fig. 15. With enhancing aging or over-aging levels, GBPs and PFZs can grow and broaden, the extent of these processes mainly depending on alloy composition, GB types, heat treatments, etc.[71·72]. For instance, the recrystallized GBs with HAGBs are normally decorated with coarse, discontinuous GBPs ($\eta$ phase) and wide PFZs, e.g., MT77 (175 °C/(600-900) min) alloy in Fig. 10. As a result, the HAGBs become not only the stress or strain concentration regions, but also are easily corroded because of different corrosion potentials among GBPs, PFZs and Al matrix [73–75]. The retrogression treatments mainly aim to separate the continuous GBPs into discrete ones (Fig. 10) while partially dissolving intragranular precipitates. However, most RRA processes with the first T6 peak aging stage do not adequately dissolve larger precipitates, such as platelet $\eta'$ phase, which likely transforms into stable $\eta$ phase, causing a higher electrical conductivity at the expense of strength. For practical application of RRA process, decreasing retrogression temperature equals reduction of the driving force for precipitation or coarsening, which can slow down the precipitation or coarsening process and help prolong retrogression time, being suitable for (mid-)thick plates.

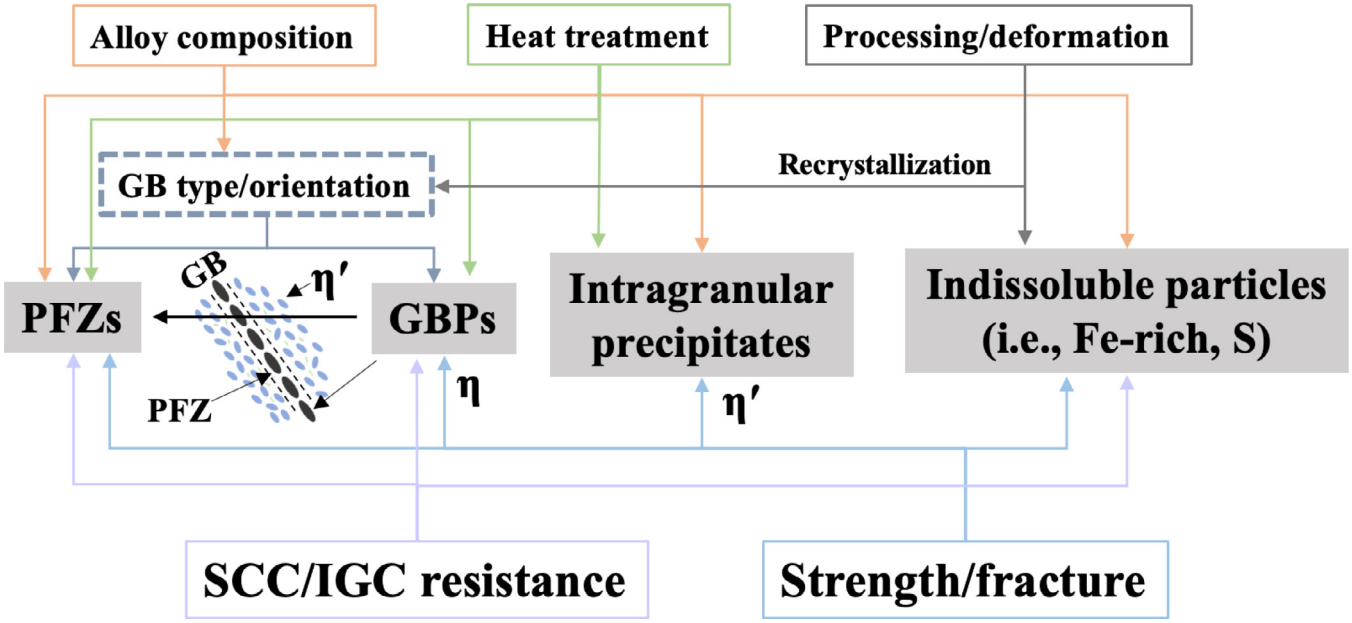


**Fig. 15.** Schematic connection between composition, process, microstructure and properties for high-strength Al alloys.

## 4. Overview of RRA treatment and future research

High-strength 7XXX-series Al alloys are hardened by uniformly distributed, high-number density and fine precipitates such as $\eta'$ phase and GP zones (Fig. 2), as the difficult-to-shear $\eta'$ phase can retard dislocation moving while GP zones are relatively easy to be sheared. However, the continuous anode GBPs (relative to Al matrix) formed in the peak-aged state (normally after T6 aging) can lead to high SCC sensitivity or inferior corrosion resistance (as shown in Fig. S3) along with affecting the fracture toughness[7·8], while their sizes, number density, and distribution can be controlled by alloy composition, aging process, grain structure, etc. As a result, these peak-aged alloys cannot be safely used for high-stress and corrosion environments such as aqueous/salt solution or moist air. Two-step over-aging processes such as T73 and T74 were designed to improve the corrosion resistance via tailoring intragranular/intergranular precipitates, but with a 10%-15% strength loss compared to the T6 state[12–14], which may be more pronounced in alloys with a higher quenching sensitivity. New generation 7XXX-series Al alloys such as AA7037, AA7040, AA7085, AA7099, AA7449 are developed with higher alloying levels and systematical design of Zn/Mg ratios and Cu concentrations[76] in a bid to obtain (mid-)thick plates with higher strength and better damage tolerance in comparison with the legacy AA7075 and AA7050 Al alloys. However, recent studies reveal that these new alloys are more sensitive to hydrogen environmentally assisted cracking in moist air[77·78], and their strength and SCC resistance highly depend on intragranular/intergranular precipitates that can be affected by alloy compositions and heat treatments. Simultaneously ameliorating the strength and corrosion resistance of 7XXX-series Al alloys, such as AA7050, would be greatly desired, for example, by modifying the precipitates via optimizing aging process as stated above.

It was reported that the two-step over-aging process can promote coarsening and discontinuous distribution of GBPs (or increasing their spacings), as irreversible hydrogen trapping points, which can not only help eliminate the continuous corrosion paths but also reduce the hydrogen concentration near GBs or hydrogen attack to the matrix, subsequently delaying crack initiation/propagation as well as enhancing corrosion resistance[8·79·80]. Meanwhile, the coarsening of intragranular precipitates can help wave slip or reduce plane slip, thereby improving the fatigue resistance[62] that is also affected by solute segregation, PFZs width and other factors[45·81]. Based on the effects of peak aging and two-step over-aging processes on the properties and precipitation, Cina et al [15]. developed an RRA process with higher retrogression temperature and shorter retrogression time, resulting in intragranular precipitates similar to T6 state and GBPs features close to those of the two-step over-aged state (see Fig. 2), for integrated high strength and better SCC resistance. These high-temperature, short-time retrogression treatments can efficiently dissolve intragranular metastable phases induced by previous peak aging for a higher solute concentration in the matrix, enabling subsequent reprecipitation of $\eta'$ phase and GP zones after the third-step aging for strengthening. At the same time, the continuous GBPs in peak-aged state change into discontinuous ones for ensuring good corrosion resistance[17·19·20·82]. The evolution of strength during retrogression (at 200 °C) and final-step peak aging (such as T6 aging at 120 °C) is schematically shown in Fig. 16(a) and the detailed description can be found elsewhere[16·18·27-29·36]. It should be noted that the retrogression treatments at 200-280 °C take only tens of seconds or minutes, being suitable for thin sheets but hardly applicable to (mid-)thick plates. Some studies decreased retrogression temperature to 170-220 °C and prolonged retrogression time to tens of minutes, leading to good corrosion resistance and high strength[17·19·20·24·82·83]. On the other hand, Jiang et al [84]. reported that it required ~120 min to uniformly approach the setting temperature across the plate thickness for a 30-mm thick Al alloy plate, and putting samples into the furnace after approaching the setting temperature would lead to non-isothermal aging during early stages, which would be even more pronounced for thicker plates. Thus, the RRA process with short-time retrogression treatment cannot ensure sufficient heating time in the plate center, and, therefore, is not applicable to (mid-)thick plates. Also, the thick plates along with the quenching sensitivity issue[85·86] have much less positive effects of the RRA process, which would be one of the key reasons for developing new alloys with a low quenching sensitivity.

The RRA process was exploited for achieving both high strength close to that of T6 state and better SCC resistance similar to that

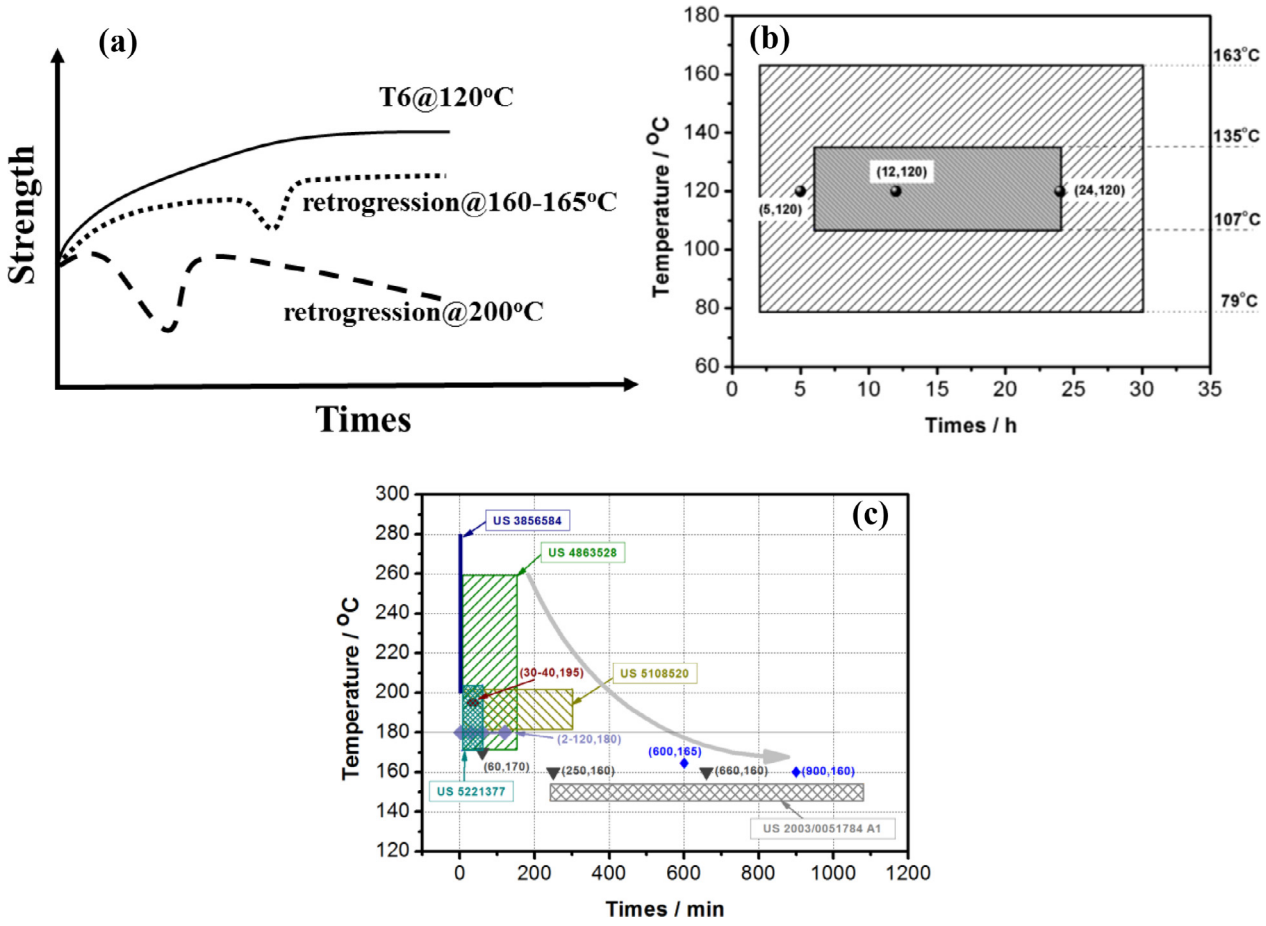


**Fig. 16.** Schematical evolution of strength during retrogression and T6 re-aging treatments (a), and aging temperature and time ranges of typical two-step aging and RRA processes: (b) first and/or third steps (the dark area represents the first and/or third step aging parameters), (c) second or retrogression step of different RRA processes.

of the T73 state, but it was found that this could not be achieved even though the strength of RRA-treated alloys might be higher than that of the T6 state[87]. This indicates that the retrogression time corresponding to the minimum retrogressed strength (Fig. 16(a)) cannot ensure concurrently high strength and good SCC resistance. Some RRA processes with lower retrogression temperature [34·83·88-91] (i. e., 160-180 °C or below 160 °C) were developed to decrease or impede the reaction dynamics during retrogression and prolong the retrogression time to ensure efficient enough holding time in the plate center. This discloses that the crucial retrogression step not only determines the dissolution of precipitates formed by previous aging, but also affects the sizes, distribution of GBPs and evolution of partial intragranular precipitates. For most RRA processes with first-step peak aging (normally 24 h) causing precipitates with a wide size distribution[5], only coherent GP zones (including solute clusters) and fine $\eta'$ precipitates can be dissolved into the matrix during retrogression at higher temperature, and larger $\eta'$ precipitates (above critical size) may grow and transform into equilibrium $\eta$ phase[92] Fig. 13. shows that the solvus or the dissolution temperature of GP zones is 130-150 °C and can go up to 170 °C[93–96], but the dissolution of GP zones cannot be achieved at Zn>5.5 wt% and Cu>1.0 wt%[30]. Thus, although some larger GPII zones with critical sizes could be transformed into $\eta'$ phases with increasing retrogression temperature via internal ordering, these transformed $\eta'$ phases may remain small and coherent with the matrix and redissolve into the matrix with further retrogression treatment. However, with relatively low retrogression temperatures such as in this study, the GP zones and fine metastable $\eta'$ particles transformed from them cannot be stably retained, while relatively larger $\eta'$ precipitates being preserved. As a result, $\eta'$ (in peak-aged alloys) to $\eta$ phase transformation during low-temperature retrogression may be possible because the solvi of $\eta'$ (250 °C) and $\eta$ (370 °C)[95] phases are obviously higher than normal retrogression temperature.

It has been shown that YS and UTS of an AA7475 Al alloy plate with 8-mm thickness after 120 °C/300 min+165 °C/900 min aging are 10.5% and 7.3% lower than those of T61 state[94·97], respectively, and also lower than those of the mid-thick AA7475-T651 Al alloy plates (6.35-12.675 mm)[98], but with better SCC resistance relative to that of T6 state. It can be deduced that this two-step aging can produce substantial strengthening precipitates and discontinuous GBPs, but the strength discrepancy relative to the T6 state reveals that the intragranular precipitates assure the properties of T6 state at the moment, and further improvement is possible via diminishing the matrix solubility for finer precipitates. In our study, partial RRA processes can be considered as a combination of the third-step aging (120 °C/24 h) and a modified version of this two-step aging process with the first-step underaging (120 °C/300 min). Table S1 shows that GPI/II zones and/or $\eta'$ phase appear in the underaged AA7XXX-series Al alloys, i.e., GPI zones and platelet $\eta'$ particles precipitate in the AA7050 Al alloy after 120 °C/360 min aging and prolonging aging time to 480 min increases the number of $\eta'$ phases[68]. Thermodynamic calculation indicates that during 120 °C/360 min aging of a quenched Al-Zn-Mg-Cu alloy, the precipitates gradually grow with a rapidly increased fraction[99], but both size and fraction remain lower than those of the peak-aged state. As a consequence, after the first-step 120 °C/300 min aging in the MT77 process, as shown in Fig. S4,

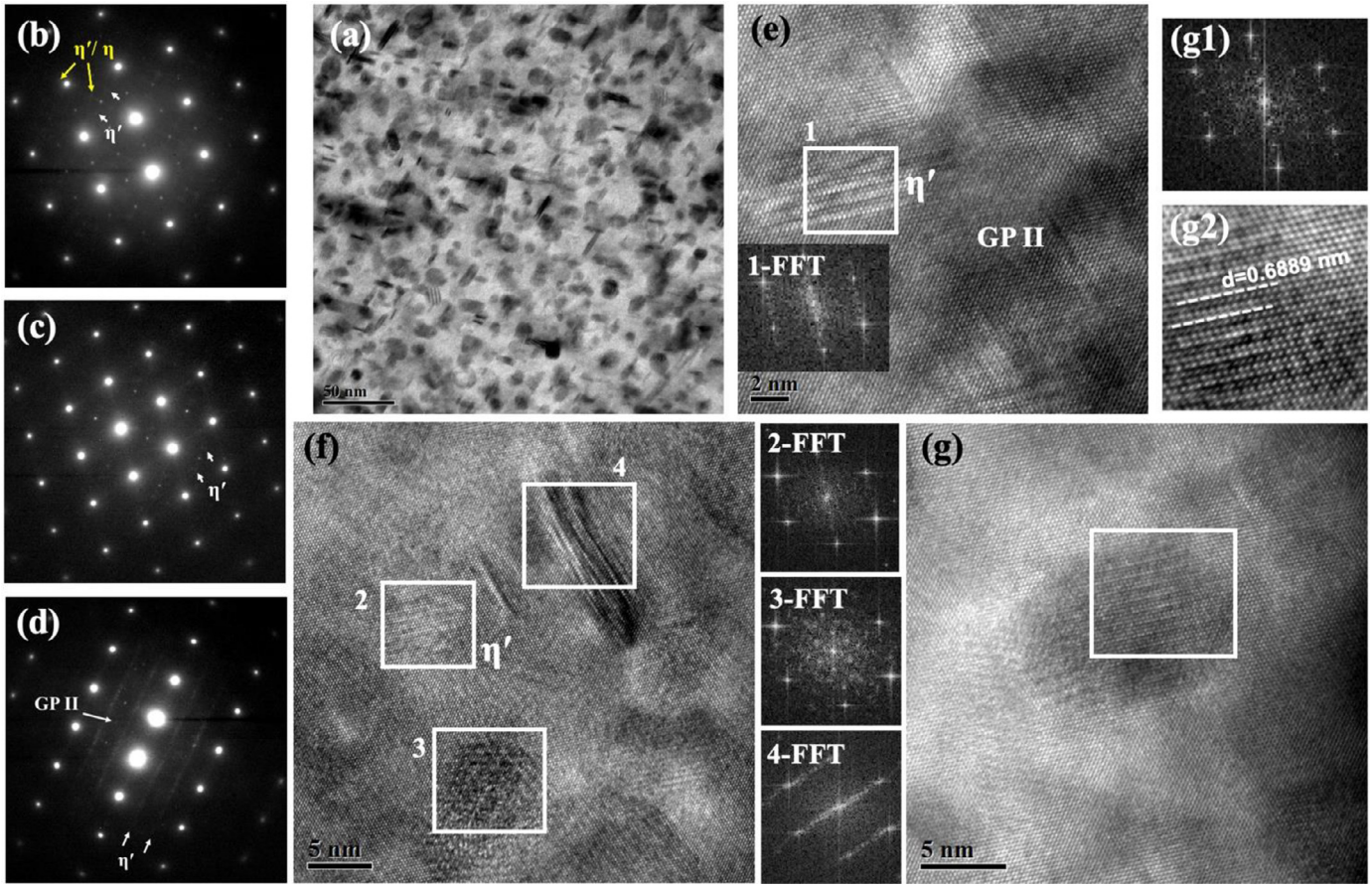


**Fig. 17.** TEM (a), SADE patterns (b-d) and HREM (e-g) images of the 165 °C/600 min retrogressed alloy with the first-step 120 °C/300 min aging. (g1) and (g2) are the FFT and IFFT images of the white-box area in (g), respectively. FFT images of other white-box areas are shown with corresponding numbers.

the sizes and amount of GP zones and $\eta'$ phase are lower than those of the peak-aged one (120 °C/1440 min), along with smaller GBPs. Then, with 200 °C as retrogression temperature, the intragranular precipitates induced by the first-step aging can be quickly and more completely dissolved into the matrix, which may facilitate the precipitation of larger $\eta'$ and even stable $\eta$ particles at 200 °C with prolonging retrogression time. However, low-temperature retrogression (i.e., 160-165 °C) may also dissolve intragranular GP zones or fine $\eta'$ precipitates induced by first-step 120 °C/300 min aging and increase solute concentration in the matrix, thus driving the growth or transformation of retained larger GP zones and $\eta'$ phase as well as new precipitates Fig. 17.(a) shows precipitates that appear in the 165 °C/600 min retrogressed alloy (with the first-step 120 °C/300 min aging) and, in general, these precipitates are distinctly coarser or grown-up as compared to those shown in Fig. 14, with most diameters below ~15 nm (Fig. S4). These precipitates are identified as $\eta'$ phase and GPII zones as well as some stable $\eta$ particles (Fig. 17 (b-d)); and the HREM images further prove the occurrence of $\eta'$ phase and GPII zone, for example, region 4 in Fig. 17(f) has similar morphology and FFT image with that in Fig. 4(h) and Fig. 8 (i, j), which could be identified as $\eta'$ phase or a transitional stage from $\eta'$ to $\eta$ phase. The FFT image of region 3 in Fig. 17(f) is similar to those in of Fig. 5(h) and Fig. 8 (f2), which is regarded as the $\eta_p$ phase Fig. 17.(g) shows another phase similar to that shown in Fig. 4(f) and the spacing between two bright single-atom layers is $d = 0.6889$ nm $\approx 3d(111)_{Al} = 0.6915$ nm, which is identified as $\eta'$ phase. Thus after 120 °C/300 min aging, GPI/II zones and finer $\eta'$ precipitates are mainly replaced by $\eta'$ phase and GPII zones. Certainly, the transformation of some larger $\eta'$ particles to stable $\eta$ phase cannot be excluded via prolonging retrogression time although it is not found, which demonstrates that low-temperature retrogression can delay this phase transformation. After the third-step re-aging, the main precipitates are $\eta'$ phase and GP zones as well as a few $\eta$ phase particles, as obtained in MT77 alloys (see Figs. 5-7), almost similar to retrogressed state, along with discretely distributed GBPs and narrow PFZs (Fig. 10). With raising retrogression temperature to 170 or 175 °C, the obviously coarsened intragranular precipitates and more $\eta$ phase in the MT77 alloys (Fig. 9) can help increase the electrical conductivity but significantly decrease the strength, approaching that of the two-step over-aging process.

Ferragut et al [100]. found that Cu addition could promote the formation of GPII zones and delay the formation of $\eta'$ phase, and high Mg content could capture more vacancies, stimulating the formation of Mg-vacancy complexes. The activation energy for GP zone formation (0.62 ± 0.03 eV) is close to that of Mg diffusion in Al matrix (0.6 eV)[101] and thus the formation of GP zones can be affected by the diffusion of Mg or Mg-vacancy complexes[102–104], as verified by Kinetic Monte Carlo simulations and experimental results[105·106]. The activation energy (0.32 ± 0.02 eV) for GP zones to the $\eta'$ phase transformation is close to the activation energy of Zn-vacancy migration (0.42 eV)[107], indicating that this transformation is correlated with the diffusion of Zn-vacancy complexes. As a result, it can be deduced that during the first-step aging of the MT77 processes, firstly Mg-vacancy complexes dominate the formation of GPI zone with Zn/Mg atom ratio <1, and then with extending aging time, for the migration of Zn-vacancy complexes, more Zn atoms can be migrated into GPI zones that sub-

sequently transform into $\eta'$ phase with Zn/Mg atom ratio >1. The fine GPI zones and $\eta'$ phase after the first-step aging (excluding individual larger $\eta'$ particles) may dissolve to increase the solute and vacancy concentration in Al matrix during retrogression at 160-165 °C. But the growth of $\eta'$ phase and/or its transformation into stable $\eta$ phase (Zn/Mg atom ratio ≈ 2[108·109]) could absorb more Zn atoms from the matrix, which makes the matrix Mg-rich. During final re-aging, the Mg-rich matrix facilitates the formation of substantial GP zones and $\eta'$ phase, which agrees well with Danh et al.[30] that an RRA process can increase the volume fraction of GP zones and $\eta'$ phase for high strength. The evolution of solute content (also with vacancies) during retrogression would be an important issue for final reprecipitation that requires exploration at these low retrogression temperatures as reported by Marlaud[36].

Based on aforementioned studies and analysis, the following ideas may benefit an RRA process for better integrated properties:

(1) T6 peak aging (i. e., 120 °C/1440 min) used usually as the first-step aging of the RRA process (such as the present T77 process) can induce the dominant $\eta'$ phase and GP zones with platelet shape and diameter around 4-6 nm[69], and during retrogression treatments, larger $\eta'$ precipitates may be grown and/or transformed into stable $\eta$ phase, weakening the final re-aging strengthening potential. Thus, the under-aging processes as the first-step aging might help avoid the formation of coarser $\eta'$ precipitates and limiting GBPs growth, in favor of controlling GBPs and relatively narrow PFZs after RRA treatments. However, Table S1 shows that the under-aging precipitates might be transformed into stable $\eta$ phase after high temperature retrogression treatments, which also depends on alloy composition, i.e., Zn/Mg ratio, Mg and/or Cu concentrations Fig. 13. shows that during low-temperature aging, GP zones require longer times to transform into $\eta'$ phase, for example, the atomic clusters (size: ~1.5 nm) formed after 85 °C/300 min aging coarsen to ~ 2.2 nm after 6000 min aging without being transformed into$\eta'$ phase[65]. But aging at above 110 °C for more than 300-360 min can promote partial transformation of GPI zones into $\eta'$ phase, and the higher the temperature, the earlier and the quicker the transformation is. If more GPII zones are formed after the first-step aging, the GPII zone-to-$\eta'$ phase transformation during retrogression treatments may be intensified. The thermodynamic calculation[99] demonstrates that during heating from the first step at 120 °C to the second step at 160 °C (similar to the first and retrogression steps of the present RRA process), the diameter and volume fraction of precipitates are obviously increased that signifies the growth and transformation of precipitates. Once the heating is done or the retrogression step starts, the precipitate growth is abated with slowly increased volume fraction, corresponding to the slowly increased strength. Further raising the second-step (retrogression) temperature enlarges the driving force for the growth of precipitates. Thus, for better controlling the precipitate states, shorter aging time is necessary Fig. 16.(b) shows the temperature/time ranges of the first step of the typical two-step aging as well as the first and third steps of an RRA process (see Table S2). For the first-step aging within time range, the GP zone, $\eta'$ and $\eta$ phases can be formed conditionally and 120 °C/300 min as the first-step aging used in this study is close to the lower limit of time range. In terms of the effect of plate thickness, the second or retrogression step displays obvious differences (Fig. 16(c)): decreasing retrogression temperature is matched with longer retrogression time. Based on the retrogression process (green region[110] in Fig. 16(c)), the retrogression temperature is decreased to 180-200 °C (dark yellow region), which helps to double retrogression time[23]. Further decreasing retrogression temperature to 145-155 °C (black region) makes retrogression time up to ~18 h, well matched with narrow aging temperature/time ranges of the first and third steps (dark area in Fig. 16(b))[92]. This makes RRA process more suitable for (mid-)thick plates and further modification of the RRA process for (mid-)thick plates may be analogous to a combination of modified T76 and T6 processes.

The present MT77 process demonstrates the feasibility to optimize the integrated properties with using first-step underaging and low-temperature retrogression, however, it seems that the dissolution of metastable GP zones and/or finer $\eta'$ phase induced by the first-step (120 °C/300 min) aging seems not to occur during the subsequent low temperature retrogression as initially intended, but instead extensive growth and/or transformation into stable phases, i.e., larger $\eta'$ phase or possible $\eta$ phase, occurs according to the above precipitate characterization. Further optimization of the first-step aging process can be performed to match well the present low-temperature retrogression treatment in order to avoid the formation of additional larger precipitates or stable $\eta$ phase. The critical size for GP zones leading to $\eta'$ and/or $\eta'$ to $\eta$ phase transformation is an important parameter that should be determined with further experiments and a quantitative analysis of volume fraction of intragranular precipitates with different sizes would be also helpful along with concurrent GBPs observation (i.e., growth and separation).

(2) The high-temperature, short-time retrogression treatments suitable for thin sheets can effectively dissolve intragranular precipitates but lead to some excessive growth and wide PFZs that should be avoided via reasonable retrogression parameters. For (mid-)thick plates, low-temperature retrogression treatments combined with the first-step under-aging can be used to adequately dissolve GP zones and fine $\eta'$ precipitates and concurrently mitigate the growth of larger $\eta'$ particles as well as their transformation into $\eta$ phase particles. This ensures high-number density of $\eta'$ phase and GP zones within grains after final re-aging along with individual $\eta$ particles. Higher Mg concentrations can not only increase the quenching sensitivity of AA7XXX-series Al alloys,[111] but also promote the formation of high-number density coherent GP zones after final re-aging, which may intensify the lattice distortion (for strengthening) and plane slip, resulting in relatively low electrical conductivity or unfulfilled SCC resistance and strain concentration during fatigue loading[42·62]. However, the interrupted T6 aging process has been proven to increase the number density of intragranular $\eta'$ phase that can well strengthen the alloy and improve elongation/toughness[112–117], and it can replace the third-step peak aging of the RRA process for obtaining high-number density fine intragranular $\eta'$ precipitates for alloys with a high Mg content that might benefit the damage tolerance.

(3) In terms of quenching sensitivity, it is helpful to determine the time required to approach the set temperature at different positions of the (mid-)thick plates, especially in plate center, which can be used as a starting time of retrogression treatment[118] to ensure efficient holding time. Additionally, as suggested by Holt[119], slight strength loss or alternative AA7XXX-series Al alloys with a higher strength and possibly a lower quenching sensitivity can be considered to meet the requirements of strength and corrosion resistance after RRA treatments. But in-depth studies and assessments are needed, especially for the new generation high-strength AA7XXX-series alloys.

It should be noted that the coarsened, discretely distributed GBPs might not be the only reason for the improved corrosion resistance using the two-step overaging or RRA process[52]. Some studies found that this could be intimately connected with Cu content of GBPs: increasing Cu content of GBPs can decrease potential difference with adjacent areas so as to diminish galvanic corrosion rate[39·53·120]. This connection between GBP composition and corrosion resistance of the MT77 alloys will be the follow-up research, as well as the effects of GB types on the evolution and distribution of GBPs, e.g. through using thermodynamic analysis[121·122]. Certainly, the MT77 process ensuring appropriate intragranular precipitates can improve the microchem-

ical properties of GBPs. However, after over-aging almost all Zn atoms near GBs take part in the formation of GBPs but only ~40% Mg atoms exist within GBPs, other free Mg atoms may capture hydrogen atoms to form Mg-H complexes that decrease GB fracture energy and make GB H-rich, which will promote GB embrittlement and stimulate stress corrosion as well as the growth of corrosion-fatigue cracks[123–126]. Thus, the effect of Mg segregation near GBs should be of particularly concern for alloys with a high Mg level although it can considerably increase the strength. It is known that one of the purposes of retrogression treatment is to promote the discrete distribution of GBPs along with coarsening, and thus unsuitable retrogression treatments may cause excess growth of local GBPs such as along HAGBs. This may induce wider PFZs and severe element segregation near GBs such as Mg atoms, being detrimental to localized corrosion resistance. If the GBPs can be controlled to an appropriate condition after the first-step aging of an RRA process, i.e., underaging state, later growth of $\eta'$ phase or transitional period from $\eta'$ to $\eta$ phases can be postponed with low-temperature retrogression treatments. Certainly, the recrystallization in (mid-)thick plates should be well controlled in advance. In addition, some micro-alloying elements (i.e., Cu or Ag in some alloy grades) are involved in the early atomic clustering and/or stabilizing atomic clusters/GP zones[100·101·127-129]. Thus, properly controlling these micro-alloying levels may facilitate the formation of high-number density GP zones and can modify localized microstructures near GBs such as PFZs width, segregation, GBPs size or distribution, which will be beneficial to ameliorate GB microchemical behavior or corrosion resistance. Obviously, the RRA treatments are multifactorial manipulating processes accompanied by sophisticated microstructure evolution. With realizing the temperature uniformity and quenching sensitivity of (mid-)thick AA7XXX-series Al alloy plates, the qualitative/quantitative characterization of thermodynamic and kinetic behavior of intragranular/intergranular precipitates depending on alloy compositions and aging processes will be conducive to develop controllable RRA processes for these plates or extruded/forged components.

## 5. Conclusions

It is obvious that increasing retrogression temperature or time can decrease the strength/microhardness of an RRA-treated AA7050 Al alloy while raising electrical conductivity. As indicated by the electrical conductivity above 40% IACS, the T77 process with short retrogression time can promote the formation of $\eta$ phase within grains, coarser GBPs and wider PFZs, which weakens the precipitation strengthening potential and facilitates localized deformation near GBs towards intergranular ductile fracture, subsequently diminishing the strength. However, the MT77 process with low retrogression temperature (i.e., 160-165 °C) can not only ensure high strength close to that of the T6 state and the electrical conductivity close or above 38% IACS for good corrosion resistance, but also prolong retrogression time to a dozen of hours, suitable for(mid-)thick AA7XXX-series Al alloy plates. The through-thickness yield strength above 520 MPa of an 86-mm thick 7050 Al alloy plate was obtained with optimum MT77 process along with some scatter of properties from surficial to central layers, which needs to be further studied in relation to alloy's quenching sensitivity. The dominant $\eta'$ phase and GP zones are responsible for the high strength of an MT77 alloy, while small and discretely distributed GBPs and narrow PFZs can facilitate the electrical conductivity and mitigate localized deformation as compared to a T77 alloy.

Coarser $\eta'$ precipitates after first-step peak aging used by most RRA processes will likely grow and/or transform into $\eta$ phase during retrogression treatments, leading to the final strength loss. Whereas, the first-step under-aging of the RRA process can form high-number density GP zones and fine $\eta'$ precipitates without unnecessary coarse $\eta'$ precipitates. Then, low-temperature retrogression can alleviate the formation of intragranular coarser $\eta'$ and/or $\eta$ particles along with dissolving GP zones and finer $\eta'$ precipitates as well as spacing GBPs, mitigating the strength loss after re-aging.

The sophisticated precipitate evolution during RRA treatments plays a critical role in the final integrated properties and thus, with considering the alloy quenching sensitivity, the RRA process should focus on effective manipulation of intragranular precipitates to diminish strength loss. In-depth studies should be devoted to the effects of GBPs features on corrosion resistance combined with designing alloy compositions and controlling grain structures, in order to achieve reliable RRA process for high-strength, corrosion-resistant AA7XXX-series Al alloy (mid-)thick plates or extruded/forged components.

## Acknowledgements

The authors would like to acknowledge the financial support from the Constructed Project for Key Laboratory of Beijing, China (No. BJSJ2019004), the State Key Laboratory for Advanced Metals and Materials of China (No. 2018Z-23), the Major State Research and Development Program of China (No.2016YFB0300801), and the National Natural Science Foundation of China (No. 51401016). L.G., C. M., L. Z. and J. S. are grateful for the supports from International S&T Cooperation Projects of Nanjing, China (No. 201818014). L.G. and D. E. kindly acknowledge support from BCAST for hosting L. G.. L. G. thanks support from the China Scholarship Council (CSC).

## Supplementary materials

Supplementary material associated with this article can be found, in the online version, at doi:10.1016/j.jmst.2021.10.057.

## References

[1] M.E. Fine, Metall. Trans. A 6 (1975) 625–630.
[2] J.K. Park, Metall. Trans. A 14 (1983) 1957–1965.
[3] J. Lendvai, Mater. Sci. Forum 217-222 (1996) 43–56.
[4] T. Marlaud, A. Deschamps, F. Bley, W. Lefebvre, B. Baroux, Acta Mater 58 (2010) 248–260.
[5] D.M. Liu, B.Q. Xiong, F.G. Bian, Z.H. Li, X.W. Li, Y.A. Zhang, F. Wang, H.W. Liu, Mater. Sci. Eng. A 588 (2013) 1–6.
[6] S.J. Andersen, C.D. Marioara, J. Friis, S. Wenner, R. Holmestad, Adv. Phys. X 3 (1) (2018) 1479984.
[7] M.O. Spiedel, Metall. Trans. A 6 (1975) 631–651.
[8] M. Puiggali, A. Zienlinski, J.M. Olive, E. Renauld, D. Desjardins, M. Cid, Corros. Sci. 40 (1998) 805–819.
[9] S. Osaki, D. Itoh, M. Nakai, J. Japan Inst. Light Metals 51 (2001) 222–227.
[10] F. Andreatta, H. Terryn, J.H.W. de Wit, Electrochim. Acta 49 (2004) 2851–2862.
[11] T. Marlaud, B. Malki, C. Henon, A. Deschamps, B. Baroux, Corr. Sci. 53 (2011) 3139–3149.
[12] M.U. Islam, W. Wallace, Met. Sci. J. 11 (1984) 320–322.
[13] J.A. Nock, Pa. Tarentum, US 2248185 (Jul. 8, 1941).
[14] D.O. Sprowls, J.A. Nock, US 3198676 (Aug. 3, 1965).
[15] B. Cina, R. Gan, US 3856584, Dec. (1974).
[16] R.S. Kaneko, Metal Prog 117 (1980) 41–43.
[17] R.T. Holt, V.R. Parameswaran, W. Wallace, Cana. Aeronautics Space J. 42 (1996) 83–87.
[18] Y.C. Yang, L.F. Cao, X.D. Wu, X. Tong, B. Liao, G.J. Huang, Z.A. Wang. J. Alloy. Compd. 814 (2020) 152264.
[19] O.S. Es-Said, W.E. Frazier, E.W. Lee, JOM 1 (2003) 45–48.
[20] R. Ranganatha, P. Raghothanma Rao, R.R. Bhat, B.K. Muralidhara, Int. J. Eng. Res. Sci. Technol. 3 (2011) 5646–5651.
[21] H. Zhao, B. Gault, D. Ponge, D. Raabe, Scr. Mater. 188 (2020) 269–273.
[22] M.S. Nandana, B.K. Udaya, C.M. Manjunatha, Fatigue Fract. Eng. Mater. Struct. 42 (2019) 719–731.
[23] J. Liu, M.M. Kersker, US 5108520 (Apr. 28, 1992).
[24] W.H. Hunt, J.T. Staley, D.A. Kukasak, D.B. Reiser, R.K. Wyss, L.M. Angers, US 5221377 (Jun. 22, 1993).
[25] E. Oswald, R.W. Westerlund, US 2003/0051784 A1 (Mar. 20, 2003).
[26] M. Talianker, B. Cina, Metall. Trans. A 20 (1989) 2087–2092.
[27] J.K. Park, A.J. Ardell, Metall. Trans. A 15 (1984) 1531–1543.
[28] J.K. Park, Mater. Sci. Eng. A 103 (1988) 223–231.
[29] A.F. Oliveira, M.C. de Barros, K.R. Cardoso, D.N. Travessa, Mater. Sci. Eng. A 379 (2004) 321–326.

[30] N.C. Danh, K. Rajan, W. Wallace, Metall. Mater. Trans. A 14 (1983) 1843–1850.
[31] Z.H. Li, B.Q. Xiong, Y.A. Zhang, B.H. Zhu, F. Wang, H.W. Liu, J. Mater. Process. Technol. 209 (2009) 2021–2027.
[32] G.S. Peng, K.H. Chen, S.Y. Chen, H.C. Fang, Mater. Corros. 62 (2011) 1–6.
[33] G.S. Peng, K.H. Chen, S.Y. Chen, H.C. Fang, Mater. Sci. Eng. A 528 (2011) 4014–4018.
[34] Y. Reda, R. Abdel-Karim, I. Elmahallawi, Mater. Sci. Eng. A 485 (2008) 468–475.
[35] C.P. Ferrer, M.G. Koul, B.J. Connolly, A.L. Moran, Corrosion 6 (2003) 520–528.
[36] T. Marlaud, A. Deschamps, F. Bley, W. Lefebvre, B. Baroux, Acta Mater 58 (2010) 4814–4826.
[37] T. Ramgopal, P.I. Gouma, G.S. Frankel, Corrosion 58 (2002) 687–697.
[38] S. Maitra, G.C. English, Metall. Trans. A 12 (1981) 535–541.
[39] Q.J. Meng, G.S. Frankel, J. Electrochem. Soc. 151 (2004) B271–B283.
[40] X.Y. Zhao, G.S. Frankel, Corros. Sci. 49 (2007) 920–938.
[41] R.K. Gutpa, A. Deschamps, M.K. Cavanaugh, S.P. Lynch, N. Birbilis, J. Electrochem. Soc. 159 (2012) 492–502.
[42] P. Guyot, L. Cottignies, Acta Mater 44 (10) (1996) 4161–4167.
[43] M.J. Starink, X.M. Li, Metall. Mater. Trans. A 34 (4) (2003) 899–911.
[44] T.C. Tsai, T.H. Chuang, Corrosion 52 (6) (1996) 414–416.
[45] J.K. Park, A.J. Ardell, Acta Metall. Mater. 39 (4) (1991) 591–598.
[46] D. Raizenne, X. Wu, Corrosion control using retrogression and re-gaing (RRA). in: Corrosion fatigue and environmentally assisted cracking in aging military vehicles, RTO-AG-AVT-140 (Mar. 2011).
[47] A.J. Hillel, P.L. Rossiter, Philos. Mag. B 44 (3) (1981) 383–388.
[48] J. Telesman, NASA Tech. Memo. 83626 (1984) 1–36 Apr..
[49] J.D. Robson, Mater. Sci. Eng. A 382 (2004) 112–121.
[50] X.Z. Li, V. Hansen, J. Gjonnes, L.R. Wallenberg, Acta Mater 47 (9) (1999) 2651–2659.
[51] Y.Y. Li, L. Kovarik, P.J. Phillips, Y.F. Hsu, W.H. Wang, M.J. Mills, Phil. Mag. Lett. 92 (4) (2012) 166–178.
[52] R. Goswami, S. Lynch, N.J. Henry Holroyd, S.P. Knight, R.L. Holtz, Metall. Mater. Trans. A 44 (2013) 1268–1278.
[53] A. Bendo, K. Matsuda, S. Lee, K. Nishimura, N. Nunomura, H. Toda, M. Yamaguchi, T. Tsuru, K. Hirayama, K. Shimizu, H. Gao, K. Ebihara, M. Itakura, T. Yoshida, S. Murakami, J. Mater. Sci. 53 (2018) 4598–4611.
[54] T.F. Chung, Y.L. Yang, B.M. Huang, Z.S. Shi, J.G. Lin, T. Ohmura, J.R. Yang, Acta Mater 149 (2018) 377–387.
[55] L.K. Berg, J. Gjonnes, V. Hansen, X.Z. Li, M. Knutson-Wedel, G. Waterloo, D. Schryvers, L.R. Wallenberg, Acta Mater 49 (2001) 3443–3451.
[56] J. Gjønnes, C. Simensen, Acta Metall 18 (8) (1970) 881–890.
[57] M.C. Carroll, P.I. Gouma, M.J. Mills, G.S. Daehn, B.R. Dunbar, Scr. Mater. 42 (2000) 335–340.
[58] http://som.web.cmu.edu/frames2.html
[59] T.F. Chung, Y.L. Yang, M. Shiojiri, C.N. Hsiao, W.C. Li, C.S. Tsao, Z.S. Shi, J.G. Lin, J.R. Yang, Acta Mater 174 (2019) 351–368.
[60] J.Z. Liu, J.H. Chen, X.B. Yang, S. Ren, C.L. Wu, H.Y. Xu, J. Zou, Scr. Mater. 63 (2010) 1061–1064.
[61] A. Joshi, C.R. Shastry, M. Levy, Metall. Trans. A 12 (1981) 1081–1088.
[62] J. Albrecht, A.W. Thompson, I.M. Bernstein, Metall. Trans. A 10 (1979) 1759–1766.
[63] B. Morere, J.C. Ehrström, P.J. Gregson, I. Sinclair, Metall. Mater. Trans. A 31 (10) (2000) 2503–2515.
[64] , Alcoa mill products, Alloy 7050 plate and sheet (2022) https://www.yumpu.com/en/document/read/11385307/alloy-7050-plate-and-sheet-alcoa.
[65] V. Hansen, O.B. Karlsen, Y. Langsrud, J. Gjønnes, Mater. Sci. Technol. 20 (2004) 185–193.
[66] A.K. Mukhopadhyay, K.S. Prasad, Philos. Mag. Lett. 91 (2011) 214–222.
[67] J.C. Werenskiold, A. Deschamps, Y. Bréchet, Mater. Sci. Eng. A 293 (2000) 267–274.
[68] G. Sha, A. Cerezo, Acta Mater 52 (2004) 4503–4516.
[69] D. Liu, B. Xiong, F. Bian, Z. Li, X. Li, Y. Zhang, Q. Wang, G. Xie, F. Wang, H. Liu, Mater. Sci. Eng. A 639 (2015) 245–251.
[70] R. Gronsky, P. Furrer, Metall. Trans. A 12 (1981) 121–127.
[71] N.U. Deshpande, A.M. Gokhale, D.K. Denzer, J. Liu, Metall. Mater. Trans. A 29 (1998) 1191–1201.
[72] B. Cai, B.L. Adams, T.W. Nelson, Acta Mater 55 (2007) 1543–1553.
[73] R.G. Buchheit, J. Electrochem. Soc. 142 (11) (1995) 3994–3996.
[74] N. Birbilis, R.G. Buchheit, J. Electrochem. Soc. 152 (2005) B140–B151.
[75] S.P. Knight, N. Birbilis, B.C. Muddle, A.R. Trueman, S.P. Lynch, Corros. Sci. 52 (2010) 4073–4080.
[76] The aluminium association, international alloy designations and chemical composition limits for wrought aluminium and wrought aluminium alloys, Jan., 2015.
[77] European Aviation Safety Agency (EASA), Environmentally assisted cracking in certain aluminium alloys, Safety Information Bulletin 2018–04R1 (2018) https://ad.easa.europa.eu/ad/2018-04R1.
[78] U. De Francisco, N.O. Larrosa, M.J. Peel, Mater. Sci. Eng. A 772 (2020) 138662.
[79] B.L. Ou, J.G. Yang, M.Y. Wei, Metall. Mater. Trans. A 38 (2007) 1760–1773.
[80] M.S. Bhuiyan, H. Toda, Z. Peng, S. Hang, K. Horikawa, K. Uesugi, A. Takeuchi, N. Sakaguchi, Y. Watanabe, Mater. Sci. Eng. A 655 (2016) 221–228.
[81] P.N. Adler, R. DeIASI, G. Geschwind, Metall. Trans. 3 (1972) 3191–3200.
[82] T. Ohnishi, Y. Ibaraki, J. Japan Inst. Light Metals 40 (1990) 82–87.
[83] S.J. Murtha, US 5496426 (1996).
[84] J.T. Jiang, Q.J. Tang, L. Yang, K. Zhang, S.J. Yuan, L. Zhen, J. Mater. Proc. Technol. 227 (2016) 110–116.
[85] P.Y. Li, B.Q. Xiong, Y.A. Zhang, Z.H. Li, B.H. Zhu, F. Wang, H.W. Liu, Trans. Nonferrous Met. Soc. China 22 (2012) 268–274.
[86] P.Y. Li, B.Q. Xiong, Y.A. Zhang, Z.H. Li, Trans. Nonferrous Met. Soc. China 22 (2012) 546–554.
[87] K. Ural, J. Mater. Sci. 13 (1994) 383–385.
[88] K. Rajan, W. Wallace, J.C. Beddoes, J. Mater. Sci. 17 (1982) 2817–2824.
[89] B.J. Connolly, C.P. Ferrer, M.G. Koul, A.L. Moran, Utilization of low temperature retrogression and re-aging (RRA) heat treatments to improved strength/SCC properties for thick section components of aluminium alloy 7075 for aging aircraft refurbishment, in: 2002 NACE Conference Papers, Colorado, Apr. (2002) 7–11.
[90] W.H. Hunt, J.T. Staley, D.A. Lukasak, D.B. Reiser, R.K. Wyss, L.M. Angers, M.H. Brown, J. Liu, S. Lee, EP 0377779B2 (Jul. 1990).
[91] D.K. Denzer, D.J. Chakrabarti, J. Liu, L.E. Oswald, R.W. Westerlund, US 0051784 (2003).
[92] F. Viana, A.M.P. Pinto, H.M.C. Santos, A.B. Lopesc, J. Mater. Process. Technol. 92-93 (1999) 54–59.
[93] H. Inoue, T. Sato, Y. Kojima, T. Takahashi, Metall. Mater. Trans. A 12 (1981) 1429–1434.
[94] L.B. Ber, Mater. Sci. Eng. A 280 (2000) 91–96.
[95] P.K. Poulose, J.E. Morral, A.J. McEvily, Metall. Trans. 5 (1974) 1393–1400.
[96] H. Löffler, I. Kovács, J. Lendvai, J. Mater. Sci. 18 (1983) 2215–2240.
[97] Properties and selection: Nonferrous alloys and special-purpose materials, 2, 10th ed., ASM Handbook, Materials Park, Ohio, 1990.
[98] Alcoa mill products, Alloy 7475 plate and sheet (2022) https://www.spacematdb.com/spacemat/manudatasheets/alloy7475techplatesheet.
[99] W.X. Shu, L.G. Hou, C. Zhang, F. Zhang, J.C. Liu, J.T. Liu, L.Z. Zhuang, J.S. Zhang, Mater. Sci. Eng. A 657 (2016) 269–283.
[100] R. Ferragut, A. Somoza, A. Dupasquier, J. Phys.: Condens. Matter 10 (1998) 3903–3918.
[101] R. Ferragut, A. Somoza, A. Dupasquier, J. Phys.: Condens. Matter 8 (1996) 8945–8952.
[102] G. Dlubek, R. Krause, O. Brümmer, F. Plazaola, J. Mater. Sci. 21 (1986) 853–858.
[103] G. Dlubek, Cryst. Res. Technol. 19 (1984) 1319–1324.
[104] G. Dlubek, W. Gerber, Phys. Status Solidi b 163 (1991) 83–89.
[105] G. Sha, A. Cerezo, Acta Mater 53 (2005) 907–917.
[106] S. Ceresara, P. Fiorini, Mater. Sci. Eng. 10 (1972) 205–210.
[107] A. Dupasquier, P. Folegati, A. Rolando, A. Somoza, S. Abis, Mater. Sci. Forum 175-178 (1994) 351–354.
[108] A. Deschamps, A. Bigot, F. Livet, P. Auger, Y. Bréchet, D. Blavette, Philos. Mag. 81 (2001) 2391–2414.
[109] M. Dumont, W. Lefebvre, B. Doisneau-Cottignies, A. Deschamps, Acta Mater 53 (2005) 2881–2892.
[110] M.H. Brown, J.T. Staley, J. Liu, S. Lee, US 4863528 (1989).
[111] D.J. Chakrabarti, J. Liu, J.H. Goodman, G.B. Venema, R.R. Sawtell, C.M. Krist, R.W. Westerlund, US 8524014 B2 (2013).
[112] R.N. Lumley, I.J. Polmear, A.J. Morton, US 7025839 (2006).
[113] J. Buha, R.N. Lumley, A.G. Crosky, Mater. Sci. Eng. A 492 (2008) 1–10.
[114] Y. Chen, M. Weyland, C.R. Hutchinson, Acta Mater 61 (2013) 5877–5894.
[115] M.E. Burba, M.J. Caton, S.K. Jha, C.J. Szczepanski, Metall. Mater. Trans. A 44 (2013) 4954–4967.
[116] L.O.R. Lima, S.C. Jacumasso, C.O.F. Terra Ruchert, J.P. Martins, A.L.M. Carvalho, Fatigue 2014, Melbourne, Australia, Mar. (2014) 2–7.
[117] Y.Q. Chen, W.W. Song, S.P. Pan, W.H. Liu, J. Central South Univ. (Sci. & Tech.) 47 (2016) 3332–3340.
[118] C. Loader, B.R. Crawford, A. Shekhter, Retrogression and re-ageing in-service demonstrator trial: stage II component test report, DSTO-TR-2686 (Mar. 2012).
[119] R.T. Holt, M.D. Raizenne, W. Wallace, D.L. DuQuesnay, RRA heat treatment of large Al 7075-T6 components, in: RTO AVT Workshop on “New Metallic Materials for the Structure of Aging Aircraft”, Corfu, Greece, Apr. (1999) 19–20.
[120] N.J. Henry Holroyd, G.M. Scamans, Metall. Mater. Trans. A 44 (2013) 1230–1253.
[121] Q. Luo, Y.L. Guo, B. Liu, Y.J. Feng, J.Y. Zhang, Q. Li, K.C. Chou, J. Mater. Sci. Technol. 44 (2020) 171–190.
[122] C.L. Liu, A. Garner, H. Zhao, P.B. Prangnell, B. Gault, D. Raabe, P. Shanthraj, Acta Mater 214 (2021) 116966.
[123] J.M. Chen, T.S. Sun, R.K. Viswanadham, J.A.S. Green, Metall. Trans. A 8 (1977) 1935–1940.
[124] R.K. Viswanadham, T.S. Sun, J.A.S. Green, Metall. Trans. A 11 (1980) 85–89.
[125] R.G. Song, M.K. Tseng, B.J. Zhang, J. Liu, Z.H. Jin, K.S. Shin, Acta Mater 44 (1996) 3241–3248.
[126] R.G. Song, W. Dietzel, B.J. Zhang, Acta Mater 52 (16) (2004) 4727–4743.
[127] J.T. Staley, R.H. Brown, R. Achmidt, Metall. Trans. 3 (1972) 191–199.
[128] T. Ogura, S. Hirosawa, A. Cerezo, T. Sato, Acta Mater 58 (2010) 5714–5723.
[129] T. Ogura, T. Sato, J.Japan Inst, Light Metals 63 (2013) 196–203.